Master's thesis

Atmospheric sciences
Remote sensing

Aerosol depolarization ratio at 1565nm in Finland with Halo Doppler lidar

Viet Le

2021

Supervisor (-s): Ville Vakkari
Examiners: Ville Vakkari, Dmitri Moisseev

University of Helsinki
Faculty of Science

HELSINGIN YLIOPISTO
HELSINGFORS UNIVERSITET
UNIVERSITY OF HELSINKI
MATEMAATTIS-LUONNONTIETEELLINEN TIEDEKUNTA
MATEMATISK-NATURVETENSKAPLIGA FAKULTETEN
FACULTY OF SCIENCE

Tiedekunta – Fakultet – Faculty Faculty of science	Koulutusohjelma – Utbildningsprogram – Degree programme Master's Programme in Atmospheric Sciences	
Opintosuunta – Studieinrikting – Study track Remote sensing		
Tekijä – Författare – Author Viet Le		
Työn nimi – Arbetets titel – Title Aerosol depolarization ratio at 1565nm in Finland with Halo Doppler lidar		
Työn laji – Arbetets art – Level Master's thesis	Aika – Datum – Month and year 05/2021	Sivumäärä – Sidoantal – Number of pages 58

Tiivistelmä – Referat – Abstract

Atmospheric aerosol particles absorb and scatter solar radiation, directly altering the Earth's radiation budget. These particles also have a complex role in weather and climate by changing cloud physical properties such as reflectivity by acting as cloud condensation nuclei or ice nuclei. Aerosol particles in the boundary layer are important because they pose a negative impact on air quality and human health. In addition, elevated aerosol from volcanic dust or desert dust present an imminent threat to aviation safety.

To improve our understanding of the role of aerosol in influencing climate and the capability to detect volcanic ash, a ground-based network of Halo Doppler lidars at a wavelength of 1565 nm is used to collect data of atmospheric vertical profiles across Finland. By comparing the theoretical values of depolarization ratio of liquid clouds with the observed values, bleed through of each lidar is detected and corrected to improve data quality. The background noise levels of these lidars are also collected to assess their stability and durability. A robust classification algorithm is created to extract aerosol depolarization ratios from the data to calculate overall statistics.

This study finds that bleed through is at 0.017 ± 0.0072 for the Uto-32 lidar and 0.0121 ± 0.0071 for the Uto-32XR lidar. By examining the time series of background noise level, these instruments are also found to be stable and durable. The results from the classification algorithm show that it successfully classified aerosol, cloud, and precipitation even on days with high turbulence. Depolarization ratios of aerosol across all the sites are extracted and their means are found to be at 0.055 ± 0.076 in Uto, 0.076 ± 0.090 in Hyytiala, 0.076 ± 0.071 in Vehmasmaki and 0.041 ± 0.089 in Sodankyla. These mean depolarization ratios are found to vary by season and location. They peak during summer, when pollen is abundant, but they remain at the lowest in the winter. As Sodankylä is located in the Artic, it has aerosols with lower depolarization ratio than other sites in most years. This study found that in summer, aerosol depolarization ratio is positively correlated with relative humidity and negatively correlated with height. No conclusion was drawn as to what processes play a more important role in these correlations.

This study offers an overview of depolarization ratio for aerosol at a wavelength of 1565 nm, which is not commonly reported in literature. This opens a new possibility of using Doppler lidars for aerosol measurements to support air quality and the safety of aviation. Further research can be done test the capability of depolarization ratio at this wavelength to differentiate elevated aerosol such as dust, pollution, volcanic ash from boundary layer aerosol.

Avainsanat – Nyckelord – Keywords
Doppler lidars, Aerosol depolarization ratio

Säilytyspaikka – Förvaringställe – Where deposited
Kumpula Science Library

Muita tietoja – Övriga uppgifter – Additional information

Acknowledgements

I want to express my immense gratitude to Professor. Dmitri Moisseev for introducing me to physics of the atmosphere, and for recommending me for the internship at Finnish Meteorology Institute.

I am grateful to have Dr. Ville Vakkari as a supervisor for my thesis and my internship at the Finnish Meteorological Institute. This thesis would not have been possible without his advice, guidance and valuable comments. I am very thankful for having such a good adviser who gave endless helps.

I also would like to thank all my friends for giving me such wonderful memories and experience at Helsinki University. A special thanks to Hannah Lobo for giving me bleed through data and for being the best colleague, friend, climbing buddy, hairdresser and baker.

I want to thank the Finnish Meteorological Institute (FMI) for offering me everything I needed to conduct this study. Financial support by National Emergency Supply Agency in Finland is also gratefully acknowledged.

Finally, I do not have enough words for the most important people in my life, my family, who continuously believed in me, no matter what, and even when I did not. Thank you.

Contents

Chapter 1

Introduction

Atmospheric aerosols are suspensions of liquid, solid, or mixed particles in the air with widely variable chemical compositions and sizes ranging from ca. one nm to tens of μm (Putaud et al., 2010).

The formation of aerosol can be categorized into two types: primary aerosol and secondary aerosol. Primary aerosol, which is emitted directly to the atmosphere, can come from natural processes such as sea spray, mineral dust, volcanoes eruption, or from anthropogenic processes such as combustion and biomass burning. On the other hand, secondary aerosol, which is produced from precursor gases in the atmosphere, can come from condensation of vapours on pre-existing particles or nucleation of new particles (Myhre, Myhre, Samset, & Storelvmo, 2015). Those precursor gases originate from both natural and anthropogenic processes. Occasionally volcanic eruptions result in huge amounts of primary and secondary aerosols in the troposphere and stratosphere (Boulon, Sellegri, Hervo, & Laj, 2011).

Aerosols can be removed from the atmosphere by two mechanism: dry deposition to the Earth's surface or wet deposition through precipitation. This leads to residence times of particles in the troposphere vary only from a few days to a few weeks (Seinfeld & Pandis, 2016). On the other hand, stratospheric aerosol can have much longer lifetime in the order of years. By coagulation, condensation, hygroscopic growth and chemical reactions, aerosol particles can evolve with time, change their size, morphology, phase, chemical composition and reactivity and other parameters such as its refractive index. Different aerosol particles with distinct composition, and size distribution have varying impacts in the atmosphere.

Aerosols can impact the climate in two ways: directly changing the Earth's radiation budget through scattering or absorbing solar radiation; or altering cloud properties by acting as cloud condensation nuclei or ice nuclei (Koch et al., 2009). Aerosols scatter or absorb sunlight to varying degrees, depending on

their physical properties. Scattering aerosols such as sulphates, nitrates and sea salt have cooling effects, by increasing reflected solar radiation from the Earth. This can have a major impact on the climate for an extended period of time. A good example is the eruption of Mount Pinatubo in the Philippines (McCormick, Thomason, & Trepte, 1995). It ejected a huge amount of sulfur dioxide into the stratosphere, and then formed sulfate aerosols. Since they remained suspended for a long period of time in the stratosphere, were dispersed around the globe by wind and did not get washed out by rain in the troposphere, these reflective particles cooled the Earth for two years afterward (McCormick et al., 1995). On the other hand, strongly absorbing aerosols like black carbon can have a warming effect by retaining the radiation heat from the sun (Bond et al., 2013). The radiative effect of deposition of absorbing aerosol depends on surface albedo. When black carbon aerosols from forest fire deposit on top of bright surfaces such as snow, ice sheets or marine stratocumulus cloud, they reduce the surface albedo, which leads to greater surface heating and more ice melting (Kaspari, Skiles, Delaney, Dixon, & Painter, 2015; Reynolds et al., 2020; Yang, Xu, Cao, Zender, & Wang, 2015). In contrast, depositions of absorbing aerosols over an already dark surface like cloud-free ocean do not have such enhanced heating effects. The highly nonuniform geographic and vertical distribution of aerosol further complicate quantification of their effects. At the result, the effects of aerosol on climate, clouds and radiative balance of the Earch are still uncertain in literature (IPCC, 2013).

Furthermore, aerosols near the surface can have severe negative impact on air quality and human health (Al-Saadi et al., 2005). Poor air quality impairs visibility and damage vegetation, it is also the cause and aggravating factor of many respiratory diseases and lung cancer (Jiang, Mei, & Feng, 2016). On the other hand, elevated aerosol layers such as those from volcanic ash plumes (Albersheim & Guffanti, 2009; Bolić & Sivčev, 2011; Guffanti, Casadevall, & Budding, 2010; Hirtl et al., 2020) or desert dust (Middleton, 2017), present an imminent threat to aviation. Fine ash aerosols, especially those with diameters below 63 µm, can be transported over very long distances (Durant et al., 2012; Prata, Carn, Stohl, & Kerkmann, 2007). This can result in a hazardous environment for aviation and can even cause impact in regions far away from the volcanic eruption. These aerosol layers can lead to poor visibility that cause considerable consequences to flight operations. They can also damage aircraft surface and engine (Eliasson, Watson, & Weber, 2016) which drastically reduce flight safety. One of the recent major incident was the eruption of Eyjafjallajökull volcano in Iceland in April and May 2010 (Gudmundsson et al., 2012; Stohl et al., 2011). This crisis caused major interruptions and a significant collapse of the air traffic system over Europe for days (Bolić & Sivčev, 2011). The resulting economic impact was enormous (International Air Transport Association, 2010) with over 104000 flights cancelled (Alexander, 2013). Although these kind of events are rare, they can have severe impacts on the environment and economy. High resolution data of aerosol vertical and horizontal distribution could play a crucial role to mitigate the impact of hazardous aerosol emissions for the avi-

ation industry (Hirtl et al., 2020). One of the motivations for this study is to improve the security of supply by air traffic in Finland by better volcanic ash detection.

Due to relatively short residence times in the troposphere, transportation by wind and the non-uniform geographic distribution of aerosol sources, the concentration and composition of tropospheric aerosol varies drastically across the world (Seinfeld & Pandis, 2016). Active remote sensing lidars enable characterization of aerosol and monitor its vertical, horizontal and temporal distribution. Space-borne lidars such as CALIPSO (Cloud-Aerosol Lidar and Infrared Pathfinder Satellite Observation; (Winker et al., 2009)) and future mission EarthCARE (Earth Clouds, Aerosols and Radiation Explorer; (Illingworth et al., 2015) cover the globe but with low temporal and spatial resolution (Baars, Seifert, Engelmann, & Wandinger, 2017). Airborne lidars, such HSRL-1 (High Spectral Resulution Lidar) built and operated by NASA Langley Research Center (Hair et al., 2008), provide good spatial coverage and fast data acquirement but is costly and only able to operate for a short period of time.

Ground-based networks of lidars, such as Finland's ground-based remote-sensing network (Hirsikko et al., 2014) provide long term in-situ continuous profiling of the atmosphere. They are able to monitor almost in real-time vertical distribution of aerosol at multiple locations. These vertical aerosol profiles facilitate the detection of elevated aerosol layers and understanding of vertical atmospheric properties throughout seasons. Halo Doppler lidars are part of the core instruments in this network.

Halo Doppler lidars (Pearson, Davies, & Collier, 2009) are fibre-optic lidar systems that operate at 1565nm, which enable long term observation of radial Doppler velocity; co- and cross- polarized signal-to-noise ratio (co-SNR, cross-SNR). From those SNR values, depolarization ratio and attenuated backscatter can be derived. With the recently developed background correction algorithm by Vakkari et al. (2019), data from much weaker signals such as from aerosol can be utilized more. Comparing to currently used Raman lidars, Halo Doppler lidars provide depolarization ratio at an additional wavelength of 1565nm and are able to operate 24/7 to provide continuous measurements.

One of the most important parameters to determine characteristics of aerosol is depolarization ratio (Pearson et al., 2009). It is the ratio of co-polarized and cross-polarized signal, which enables the distinguishing of spherical and non-spherical particles from each other (Baars et al., 2017; Burton et al., 2012); quantifying the distribution of different aerosol types to elevated layers (Mamouri & Ansmann, 2017). In addition, depolarization ratio enables classification of aerosol (Illingworth et al., 2015) into different categorizes such as smoke, dust, marine and ash. Often, depolarization ratios are measured using Raman lidar (Baars et al., 2016; Engelmann et al., 2016) at multiple wavelengths such as 355nm, 532nm, 710nm or 1064nm. However, this study is conducted using data from Halo Doppler lidar at 1565nm, with the aim to shed more light on aerosol properties at this wavelength following the study by Vakkari et al. (2020) using

the same instrument.

In this study, data retrieved by Halo Doppler lidars across Finland's ground based remote-sensing network (Hirsikko et al., 2014) is utilized. The aim of this study is to assess and improve the quality and stability of depolarization ratio in long-term operation of Halo Doppler lidars and obtain overall statistics of aerosol depolarization ratio at 1565nm in Finland. This can facilitate the detection of volcanic ash in Finland, and as the results, improve the security of supply in Finland by air the event of aviation disruptions such as volcanic eruptions.

Liquid clouds were identified and depolarization ratios at liquid cloud base are collected to derive the bleed through (Vakkari et al., 2020) of all Halo Doppler lidar instruments. This facilitates better estimation of the depolarization ratio accuracy and uncertainty, thus improving the reliability of future data. In addition, since the data was pre-processed by the background correction algorithm proposed by Vakkari et al. (2019), the stability of instruments was also assessed by constructing the time series of signal-to-noise ratio in aerosol and cloud free regions. On the other hand, a classification algorithm is developed that enable the separation of clouds, precipitation and aerosol. The algorithm was used to obtain overall statistics of aerosol depolarization ratio at 1565nm in Finland. This statistics can improve aviation safety by providing a baseline of depolarization ratio at this wavelength, so that potentially hazardous layers such as from volcanic ash can be separated from natural aerosol. Furthermore, this study offers views on temporal and vertical distribution of aerosol depolarization ratio in Finland, which enable future studies on aerosol interactions with climate.

Background theory of lidar along with depolarization ratio, background noise, attenuated backscatter, vertical velocity, depolarization ratio and bleed through are described in section 2.1. The measurement sites, instruments and data used are shown in section 2.2 while detail description of the classification algorithm is described in section 2.3. Section 3.1 discuss the result of instrumental stability. Section 3.2 presents overall statistics of aerosol depolarization ratio at 1565nm along with its correlation with range and humidity. Finally, the conclusion is presented in section 4.

Chapter 2

Materials and Methods

2.1 Lidar

Lidar (light detection and ranging) is a remote sensing method, which uses laser light to profile the atmosphere. Pulses of polarized laser beams are emitted into the atmosphere and the returned signal is collected in either parallel polarization (co-polar) or orthogonal polarization (cross-polar) to that of the emitted laser. By processing the return signals, characteristics of the atmosphere profile can be derived. The lidar returned signal for each polarization follows the same lidar equation (Weitkamp, 2005) as below:

$$P(R,\lambda) = P_0 \frac{c\tau}{2} A\eta \frac{O(R)}{R^2} \beta(R) exp\left[-2\int_0^R \alpha(r,\lambda)dr\right] \tag{2.1}$$

Where P is the received power, P_0 is the outgoing power, R is the distance, A is the area of receiver optics, η is the system efficiency, $O(R)$ is the overlap function, $\beta(R)$ is the backscatter coefficient and α is the extinction coefficient. For lidars that send and receive pulses through one single lens, such as Halo Stream Line Doppler lidar, there is no overlap so $O(R)$ simplifies to 1 (Hey, Coupland, Foo, Richards, & Sandford, 2011).

There are five basic lidar techniques used in atmospheric science: elastic and inelastic (Raman) lidars, differential-absorption lidars, resonance fluorescence lidars and Doppler lidars (Weitkamp, 2005). These technique are based on the different interaction processes between emitted radiation and the atmospheric constituents.

Elastic lidars are the simpliest form of lidars which utilize elastic backscattered light from atmospheric particles. In elastic scattering, the emitted wavelength

from the laser source remains unchanged after interaction with the target. Modern multiwavelength Raman lidars such as $Polly^{XT}$ have channels at 355 nm, 532 nm, and 1064 nm configured to measure elastic scattering from aerosol. They provide lidar ratio, scattering and extinction Ångström exponents, elastic backscattering and depolarization ratio continuously (Baars et al., 2016). This information allows for the classification of aerosol into mineral dust, smoke, marine aerosol and volcanic ash (Baars et al., 2017; Müller et al., 2007; Papagiannopoulos et al., 2018). In addition, calculated depolarization ratios enable determination of aerosol shape (Kanitz, Ansmann, Engelmann, & Althausen, 2013), separation of dust and non-dust particles in mixed aerosol (Baars et al., 2011), investigation of mixed-phase clouds (Kanitz et al., 2011) and determination of composition of mixed-dust layers (Baars et al., 2012; Kanitz et al., 2013; Tesche et al., 2011).

Raman lidars, as the name suggest, also utilize Raman scattering which is an inelastic scattering process of light to airborne molecules in the atmosphere. When emitted light hits a molecule, the vibrational-rotational energy level of the molecule changes (Raman & Krishnan, 1928). This causes a shift in frequency of the backscattered light which is characteristic for the scattering molecule (Weitkamp, 2005). Due to high daylight background intensity, Raman lidar observations are challenging and require assumptions about aerosol (Baars et al., 2016; Engelmann et al., 2016) during the day. Most Raman lidars measure temperature, atmospheric gases such as O_2, N_2 and water vapor.

On the other hand, Doppler lidar measures continuously the elastic backscattering of atmospheric particles, in order to derive their velocity. Generally with longer wavelength, such as 1565nm with Halo Doppler lidar, backscatter from air molecules (Rayleight scattering) is negligible, so aerosol particles or precipitations (Mie scattering) dominate the returned signal (Hirsikko et al., 2014). As the name suggest, Doppler lidars measure velocity based on the Doppler shift in the return signal after being scattered by a moving particle. In order to also determine the sign of the shift in frequency of the signal and not just its magnitude, heterodyne detection is applied (Weitkamp, 2005). Heterodyne detection (also called coherent detection) is originally developed in the field of radio waves and microwaves. Instead of passing the return signal through optical filters, in heterodyne detection, the return signal is mixed with a strong local oscillator wave and the result mixed signal contains the sum and difference of those two components. The main advantages of heterodyne detection are the capability to measure weak backscattered light with minimal Doppler shifts and high tolerance of background light (Weitkamp, 2005).

Conventionally, Doppler lidars are primarily utilized for wind related measurements, which is traced by aerosol particles movements. From these velocity measurements, turbulent profiles (O'Connor et al., 2010) and mixing layer height (Emeis, Schäfer, & Münkel, 2008) can be derived. Recently, with the development of the post-processing method by Vakkari et al. (2019) for Halo Doppler lidars, instrumental noise level can be reduced. As the result, data availabil-

ity from weak signals of aerosol can be increased, thus, depolarization ratio for aerosol at wavelength 1565nm can be utilized in Halo Doppler (Vakkari et al., 2020).

The obtained parameters used in this study from Halo Doppler lidars are co-polarized signal-to-noise-ratio (co-SNR), cross-polarized signal-to-noise-ratio (cross-SNR), attenuated backscatter (beta), vertical velocity (v) and depolarization ratio.

2.1.1 Background noise

The co-SNR and cross-SNR data in this study have been processed with a background correction algorithm proposed by Vakkari et al. (2019). The resulting background region (aerosol-cloud free) is supposed to follow Gaussian distribution with zero mean. This background noise is collected manually by going through daily data and extracting a sizable aerosol-cloud free region.

By looking at the noise level throughout seasons and years of each instrument, its stability and durability can be assessed. This plays an important role in data quality checks to make sure that equipment are not affected by harsh outdoor environments especially during winter, as long-term performance of those instruments have not been evaluated before.

2.1.2 Attenuated backscatter

Attenuated backscatter (beta) is the backscatter coefficient that affected by the atmospheric transmission and distance away from the lidar. It is calculated from the signal-to-noise ratio and requires knowledge of the telescope function. Clouds, aerosols or rain near the ground can greatly affect attenuated backscatter values as the measurements are made from the ground. For example, if two aerosol layers with the same backscatter coefficient are observed in different conditions, their attenuated backscatter would be different (e.g one on top of clean air and the other on top of a cloud).

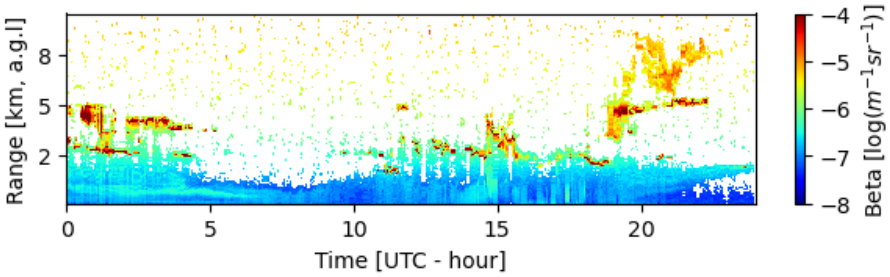

Figure 2.1: Attenuated backscatter on 2018-06-11 at Hyytiala

Figure 2.1 shows attenuated backscatter log-scaled on 2018-06-11 at Hyytiala.

Clouds are thick optically, so they generally have beta (in log space) larger than -5 while the beta values of aerosol are lower than that. However, this threshold is an arbitrary number which were selected from experience and the distinction between aerosol and clouds is getting smaller near this value.

2.1.3 Vertical velocity

Vertical velocity (called velocity from now on) is the vertical speed of particles. It is determined from the changes of frequency of emitted and returned signal. Negative velocity indicates movement towards the ground. Precipitation from rain usually has velocity less than -1 m/s while snow can have velocity less than -0.5 m/s. For aerosol, the falling velocity is negligible, and dictated mainly by winds and turbulence. Velocity in the turbulent area often ranges between -2 m/s and +2 m/s but can be more extreme.

Figure 2.2 displays velocity on 2018-06-11 at Hyytiala. The rain from 15 UTC to around 17 UTC is shown by a blue region with velocity uniformly less than -1 m/s. However, the region of aerosol from 8 UTC to 12 UTC has velocity fluctuation from positive to negative values. This can cause difficulties in distinguishing aerosol from rain in classification algorithms.

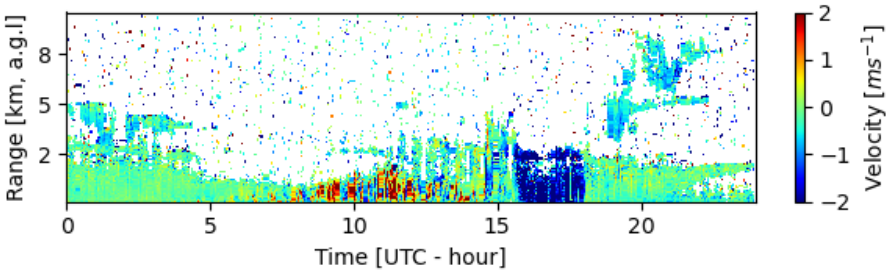

Figure 2.2: Vertical velocity on 2018-06-11 at Hyytiala

2.1.4 Depolarization ratio

Depolarization ratio is calculated as the ratio of cross-SNR to co-SNR:

$$\delta = \frac{SNR_{cross}}{SNR_{co}} \tag{2.2}$$

and its uncertainty is

$$\sigma_\delta \approx |\delta| \sqrt{\frac{\sigma_{cross}^2}{SNR_{cross}^2} + \frac{\sigma_{co}^2}{SNR_{co}^2}} \tag{2.3}$$

where SNR_{cross}, σ_{cross} and SNR_{co}, σ_{co} are observed value and standard deviation of background cross-SNR and co-SNR respectively, and δ is the depolarization ratio.

For Halo Doppler lidar instruments, due to its long wavelength 1565nm, it is considered that the measured depolarization ratio has no contribution from molecular component, hence, it is regarded as linear particle depolarization ratio (Vakkari et al., 2020)

2.1.5 Bleed through

Single scattering from a spherical droplet does not change the incident polarization state into the 180 degree backward direction (Liou & Schotland, 1971), which results in a depolarization ratio of zero. As the laser beam penetrates the cloud, the depolarization ratio gradually increases as the multi-scattering process occurs further into the cloud (Hu et al., 2006; Liou & Schotland, 1971), which is demonstrated in figure 2.3. Hence, depolarization at the cloud base would be the smallest because of the high fraction of single scattering (Sassen & Petrilla, 1986). In other words, it is expected that depolarization ratio at pure liquid cloud base is close to zero.

Bleed through in the context of depolarization ratio is defined as incomplete extinction in the lidar internal polarizer (Vakkari et al., 2020), where co-polarized signal is leaking into cross-receiver. By measuring how much the observed depolarization ratio at liquid cloud base deviates from zero, bleed through of the instrument can be determined. This is important for Halo Doppler lidar instruments as they do not facilitate the calibration of depolarization ratio, unlike aerosol research lidars such as PollyXT (Baars et al., 2011).

In order to determine the bleed through, depolarization ratio of liquid cloud base was collected at Uto in this study and at other sites by Hannah Lobo at the Finnish Meteorological Institute. Where possible, at least one cloud per week was selected. Figure 2.3 illustrates a typical liquid cloud profile. The cloud base is chosen at the range gate with the highest corresponding co-SNR, which is marked in yellow in the figure. The depolarization ratio is lowest at the cloud base and increases into the cloud due to the multi-scattering process. To distinguish cloud from aerosol below it, the highest co-SNR signal is chosen as an indication for cloud base. However, it should be noted that sometimes the highest co-SNR can be inside the cloud where multi-scattering effect already occurred. Thus, this method is utilized to quickly speed up the process, and the result is approximately an upper limit of depolarization ratio at cloud base, or so-called bleed through. By collecting the bleed through in an extended period of time, its stability in all instruments can be assessed.

The criteria for pure liquid clouds are as follows:

- Attenuated backscatter value larger than 10e-4

- Total attenuation result in thin cloud as seen by lidar instrument

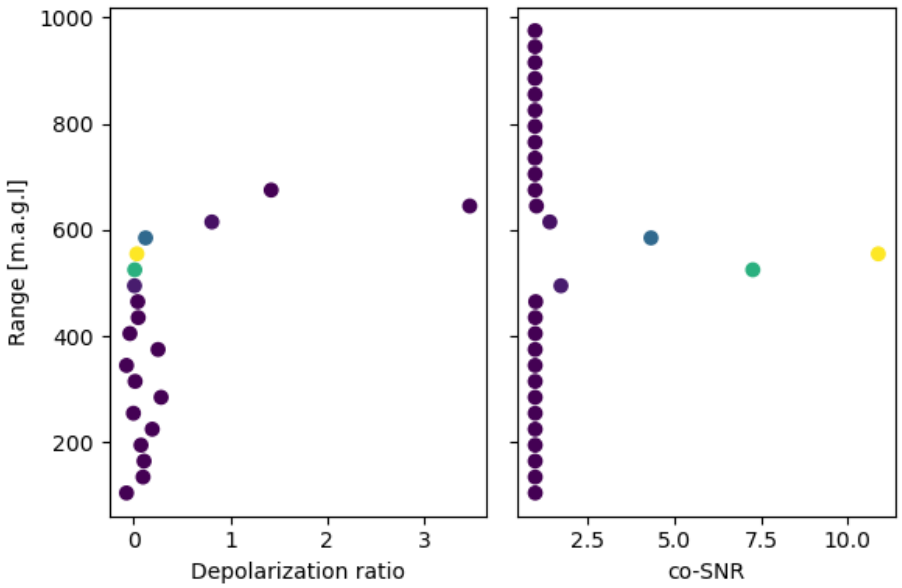

Figure 2.3: Example of a cloud profile, where maximum SNR corresponding to the cloud base with lowest depolarization value. Profile taken at 2016-02-23 17.646 UTC, Uto

- Doppler velocity close to 0 m/s as indicative of air movement

The occurrence of pure liquid clouds is highly dependent on local weather and seasonal climate. Our criteria for choosing pure liquid clouds can sometimes result in mixed phased clouds with a elevated depolarization ratio, especially in winter. Consequently, the distribution of the obtained depolarization ratio was a multimodal distribution as seen in figure 3.4. As our goal was to determine depolarization ratio of only liquid clouds, the smallest mode of the distribution was used to represent them. Standard deviation and mean of the distribution are calculated assuming Gaussian distribution. In the case of multimodal distribution, a Gaussian mixture model is used to extract only the mean and standard deviation of the mode with smaller mean. Resulting mean and standard deviation is the mean and standard deviation of bleed through of the instrument.

After depolarization at cloud base for each instrument (i.e bleed through) is collected, the cross-SNR values are corrected and depolarization ratio is recalculated as follows (Vakkari et al., 2020):

$$SNR_{cross,B} = SNR_{cross} - B \cdot SNR_{co} \tag{2.4}$$

$$\delta = \frac{SNR_{cross,B}}{SNR_{co}} \tag{2.5}$$

Where SNR_{co} and SNR_{cross} are observed co-SNR and cross-SNR respectively, B is the estimated mean bleed through (i.e mean depolarization ratio at cloud base), $SNR_{cross,B}$ is the corrected cross-SNR and δ is the depolarization ratio. The uncertainty in $SNR_{cross,B}$ and δ are estimated as:

$$\sigma_{cross,B} = \sqrt{\sigma_{co}^2 + (B \cdot SNR_{co})^2 \cdot (\frac{\sigma_B^2}{B^2} + \frac{\sigma_{co}^2}{SNR_{co}^2})} \tag{2.6}$$

$$\sigma_\delta = |\delta| \sqrt{\frac{\sigma_{cross,B}^2}{(SNR_{cross} - B \cdot SNR_{co})^2} + \frac{\sigma_{co}^2}{SNR_{co}^2}} \tag{2.7}$$

where σ_B is standard deviation of the bleed through (i.e standard deviation of depolarization ratio at cloud base), σ_{co} is the standard deviation of co-SNR of the background.

2.2 Measurements

2.2.1 Instruments

Halo Photonics StreamLine Doppler lidars (Halo Doppler lidars) are 1565nm pulsed Doppler lidars equipped with heterodyne detectors that can switch between co- and cross- channels (Pearson et al., 2009). These lidars are also fibre-optic systems, utilizing solid-state lasers, and capable of operating continuously for a long period of time (Harvey, Hogan, & Dacre, 2013). In addition, the eye-safety requirement is conformed to as they operate at high-pulse repetition and low-pulse energy mode with a 1565 nm laser (Pearson et al., 2009).

Three versions of Halo Doppler lidars are utilized in this study: Stream Line, Stream Line Pro and Stream Line XR lidars (*HALO PHOTONICS — StreamLine series - Product*, 2021). The StreamLine and StreamLine XR lidars are capable of full hemispheric scanning. Designed for harsher environments, the SteamLine Pro lidar has no moving parts, which limits the scanning to within a 20 degree cone around Zenith. The StreamLine XR has higher power and lower frequency, thus can observe up to 12km into the atmosphere compared to only 9.6km for StreamLine lidar. Key specifications of all instruments are shown in Table 2.1.

The standard operation mode of each instrument varies across time and location. The standard operation mode consists of continuous vertical staring with periodical switching to a three-beam Doppler beam swinging (old-method) or velocity-azimuth display to obtain radial velocity profiles. For about 10 seconds in every hour the instruments perform a periodical background noise determination. Only data from the vertical staring mode is utilized in this study, so

Specification	**Values**
Wave length	156 5nm
Beam divergence	3.3e-05 rad
Laser Energy	1e-05 J
Lens diameter	0.06 m
Number of samples per range gate	10
Range resolution	30 m
Pulse repetition frequency	15 kHz 10kHz for XR device
Pulse length	200 ns
Focus	2km infinity for XR device
Minimum range	90 m

Table 2.1: Standard configuration in all Halo Doppler lidar instruments

occasional gaps in data availability is due to lower elevation angle scanning and background noise check.

In the vertical staring mode, the instrument emits pulses of polarized beam laser into the atmosphere and then measures the returned signal in both co- and cross-channels (co-SNR, cross-SNR) sequentially. From these measurements, profiles of attenuated backscatter, depolarization ratio, and vertical winds are derived.

For each range gate, 10 samples (3 m resolution) are averaged to obtain observations for each 30 m range gate. Additionally, a ray is defined as the average of multiple pulses, so the higher the integration time, the more pulses in a ray. These adjustments of samples per gate and number of pulses per ray are made to balance temporal resolution and sensitivity (Hirsikko et al., 2014). The number of pulses per ray (i.e integration time) varies for each location as different sensitivities are required (e.g. Sodankylä has a clean air environment and needs a higher sensitivity than Utö which has a humid environment). However, the samples per range gate is kept constant at 10 for all locations.

In Halo Doppler lidars, measurements of co-SNR and cross-SNR are taken sequentially. For example, if the integration time of the instrument is set to 7 seconds then co-SNR signal is collected for 7 seconds and then cross-SNR signal is collected during the next 7 seconds (Vakkari et al., 2020), and the resulting co-SNR and cross-SNR will be presented at the same time stamp. Thus, if a particle is moving vertically during the switching of co- and cross-SNR signals, the depolarization ratio will not be accurate if the integration time is too long. This plays an important role in the accuracy of measurements of depolarization ratio at cloud base, since the desired measurements are only located in one certain range gate at the cloud base. However, integration time does not affect the statistics of overall aerosol since data will be averaged in bins of time and range

Site	Description	Study period
Helsinki - Kumpula (SMEAR III) $60.20^oN, 24.96^oE$	Urban	6.4.2018 - 13.9.2019 13.9.2019 - 29.10.2019: XR 5.12.2019 - 31.12.2019: XR
Utö $59.77^oN, 21.37^oE$	Island	1.1.2016 - 16.8.2017 22.11.2017-31.12.2019: XR
Vehmasmaki - Kuopio $62.89^oN, 27.63^oE$	Semi-urban/rural	1.1.2016 - 30.1.2017 17.5.2018 - 31.12
Hyytiälä (SMEAR II) $61.84^oN, 24.29^oE$	Rural (boreal forest)	1.1.2016 -7.8.2017 9.10.2017 - 31.12.2019
Sodankylä $67.37^oN, 26.62^oE$	Arctic rural	19.6.2017 - 28.11.2017 15.3.2018 - 20.11.2019

Table 2.2: Description of instrument locations (Hirsikko et al., 2014)

and we assume that aerosol is mixed well within each aerosol layer.

2.2.2 Sites

The Halo Lidar network across Finland consists of five different measurement stations (Figure 2.4). Each location has unique conditions, enabling the comparison between both urban and rural, and marine, coastal, continental, and Arctic. Detailed descriptions and the study period for each location are shown in Table 2.2.

These stations are part of Finland's ground-based remote-sensing network (Hirsikko et al., 2014). The network was established by the Finnish Meteorological Institute and University of Helsinki, with the goal of monitoring air pollution and boundary layer properties in real-time (Hirsikko et al., 2014). Halo Doppler lidars are part of the core instruments in the network.

2.2.3 Data

Data is collected continuously, from 2016 to 2019 across Finland. Details of the time period and locations are shown in table 2.2. However, data from Kumpula has found to be not at an adequate quality, and will not be used in this study. Obtained parameters for this analysis include attenuated backscatter, depolarization ratio, vertical Doppler velocity, co-polar SNR and cross-polar SNR. The typical raw data is shown in Figure 2.6, at which the x-axis is time (hour-UTC) and y-axis is height (km above ground level)

The manufacturer recommends to remove all observations with signal-to-noise-ratio (SNR) value less than 0.015 (-18.2DB) (Manninen, O'Connor, Vakkari, & Petäjä, 2016). However, the number of ambient aerosol particles is low at many network stations (Engler et al., 2007; Kulmala et al., 2001; Leskinen et al.,

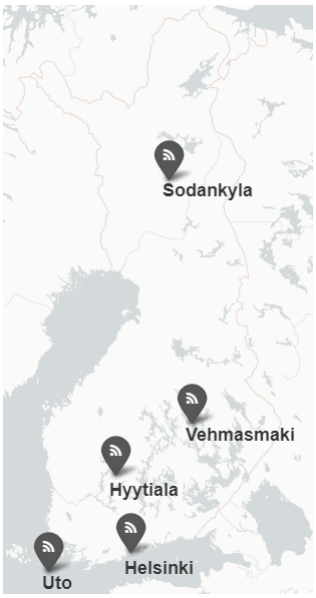

Figure 2.4: Locations of the instruments across Finland
Base map from openstreetmap.org

2011; Maso et al., 2008), apart from Helsinki (Aarnio et al., 2005; Hussein et al., 2007). Consequently, this high threshold significantly reduces data availability, especially in a clean atmosphere. Ambient aerosol can have a relatively a low cross-SNR, even as low as approximately 1 percent of its co-SNR (Illingworth et al., 2015), which makes the retrieval of cross-SNR even more challenging. Hence, a proper post-processing method is needed to utilize these weak signals of aerosol.

Data in this analysis has been processed by the background correction algorithm proposed by Vakkari et al. (2019). By identifying and correcting sources of error in SNR, this algorithm enables the averaging of long periods of time to utilize weak signals of SNR down to -32 dB. Thus, it enables the study of ambient aerosol. It is also important to note that for the Stream Line XR, its background noise level in the near range can not be determined accurately due to a more sensitive amplifier (Vakkari et al., 2019). This is a contributing factor for the bad quality data at Helsinki - Kumpula, which is discarded in this study.

However, data of the XR instrument at Utö is in a good condition, with the exception of unknown component in the near-range focus function which results in an overestimation of attenuated backscatter. Though, depolarization ratio does not get affected by by the focus function. The correction for attenuated backscatter will be discussed in section 2.3.3, which will be used in the following classification algorithm to extract depolarization from aerosol.

2.3 Classification algorithm

2.3.1 Introduction

This classification algorithm is created to separate aerosol from clouds and precipitation in the data. The primary goal is to use this algorithm on all data to determine the statistics of depolarization ratio of aerosol in Finland. By using velocity, beta and co-signal SNR fields, the algorithm classifies all data into corresponding classes:

0 : Background signal

10 : Aerosol

20 : Precipitation

30 : Clouds

40 : Unknown

Since each of the variables data has two dimensions: time and range, this algorithm uses 2D-kernel (filter) to extract features from the data. Figure 2.5 illustrates how a median filter with size 3x3 works

The main idea of median filter is to run through each data point one by one, replace its value with median of neighbouring values. Similarly, maximum filter replace its center value with the maximum of neighbouring values. The pattern of neighbor values is defined by the size of the filter, which in this case is 3x3. As shown in figure 2.5, this median filter removes noisy signal and smooth the remaining of the data.

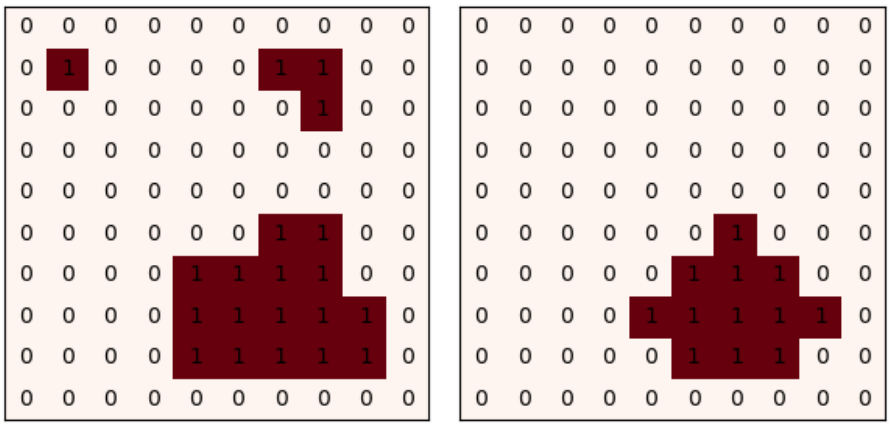

Figure 2.5: Raw data (left) and after applying median filter size 3 by 3 (right)

In addition, this classification algorithm also utilizes Density-based spatial clustering of applications with noise (DBSCAN) clustering algorithm (Ester, Kriegel,

Sander, & Xu, 1996) to fine tune aerosol classification. The goal of DBSCAN is to separate aerosol clusters based on their position in the time and range dimensions. If the aerosol data are connected together in those dimensions then they will be assigned to the same cluster.

2.3.2 Procedure

1. Load data (for illustration, data on 2018-08-12 at Hyytiala is used)
2. Preprocess data

   Remove all data with range less than 90m and correct bleed-through for cross-SNR variable. The resulting data is shown in figure 2.6

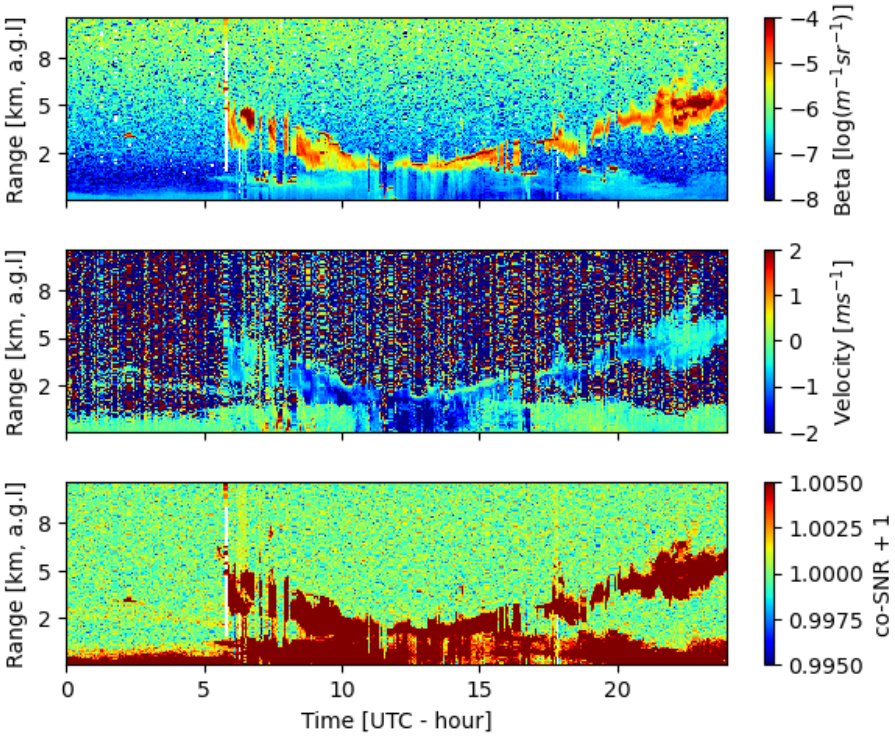

Figure 2.6: Beta, velocity, and co-signal on 2018-08-12 at Hyytiala

3. Create a classifier mask with the same side of data

   This is an empty matrix with the same size of the data. All the classifications are saved into this matrix.

Aerosol

4. Filter data with 1 standard deviation of background noise (cloud-aerosol free region) *The filter here is based on values of co-SNR and removes values of all variables if the corresponding co-SNR is less than 1 standard deviation of background noise.*

5. Aerosol masking

   (a) Create an aerosol mask by threshold all data have log-beta values less than -5.5

   (b) Apply 2D median filter with size 11 by 11 (time by range) to remove noise

   (c) Apply 2D median filter again with size 15 by 1

   (d) Apply aerosol mask to the classifier mask, the result is shown in figure 2.7

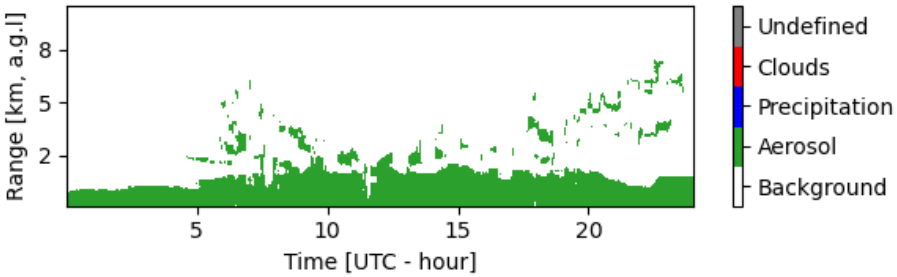

Figure 2.7: Classification mask after step 5

Cloud

6. Filter data with 3 standard deviations of background noise

   The filter here is based on values of co-SNR and removes values of all variables if the corresponding co-SNR is less than 3 standard deviation of background noise.

7. Cloud masking

   (a) Create cloud mask by threshold all data have log-beta values beta more than -5.5

   (b) Apply 2D maximum filter with size 5 by 5 to increase the size of cloud region

   (c) Apply 2D median filter with size 13 by 13 to remove noise

(d) Apply cloud mask to the classifier mask, the result is shown in figure 2.8

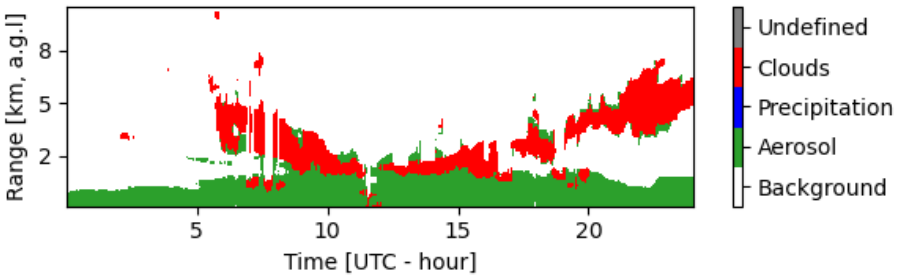

Figure 2.8: Classification mask after step 7

Precipitation

8. Updraft masking - indication of aerosol
   (a) Create updraft mask with all data have velocity more than 1 m/s
   (b) Apply 2D median filter with size 3 by 3 to remove noise
   (c) Apply 2D maximum filter with size 91 by 91 to increase the size of updraft region
   (d) Apply 2D median filter with size 31 by 31 to fill in gaps in updraft zone

   The updraft region is the region where heavy precipitation does not occur

9. Heavy precipitation masking
   (a) Create heavy precipitation mask with all data which have velocity less than -1 m/s and log-beta larger than -7
   (b) Apply 2D median filter with size 9 by 9 to remove noise
   (c) Remove all updraft masking inside heavy precipitation
   (d) Apply 2D median filter with size 3 by 3 to remove noise

   Heavy precipitation can be considered as the center of a precipitation event where the velocity of all hydrometers reach -1 m/s. In addition, since precipitation should be optically thick, a threshold of log-beta less than -7 is also applied to avoid turbulence in aerosol.

10. Precipitation masking with all data which have velocity less than -0.5 m/s and log-beta larger than -7

    This includes all precipitations, even with small negative velocity

11. Small updraft masking
    (a) Create small updraft mask with all data which have velocity more than 0.2 m/s
    (b) Apply 2D maximum filter with size 3 by 3 to increase the size of small updraft masking

    Small updraft is a region where no precipitation can occur

12. Final precipitation masking
    (a) Through 1500 iteration:
        i. Apply maximum filter with size 3 by 3 to the heavy precipitation mask (step 9)
        ii. Remove small updraft masking from the resulting mask
        iii. Combine with Precipitation mask
        iv. Stop when final precipitation mask stops growing
    (b) Apply final precipitation mask to classifier mask

    The idea of this step is to only extract clusters of precipitation in the precipitation mask that also contain values in heavy precipitation mask. Through each iteration, heavy precipitation mask grows slowly toward Precipitation mask while avoid small updraft mask. The result is the final precipitation mask. The process of this step is shown in figure 2.9.

Attenuation correction

13. Replace all aerosol above cloud and precipitation with the corresponding class

    For precipitation:

    (a) get precipitation mask from the classifier mask
    (b) Replace all aerosol class above precipitation with precipitation class

    For cloud:

    (a) Create a mask with all data have log-beta larger than -5
    (b) Apply maximum filter with size 5 by 5 to the resulting mask
    (c) Apply median filter with size 13 by 13 to the resulting mask to obtain cloud mask,
    (d) Replace all aerosol class above cloud mask with cloud class

    The goal of this step is to correct the classification for data above cloud and precipitation, which suffer from attenuation. The cloud mask was calculated again instead of using classifier mask is to avoid thick smokes

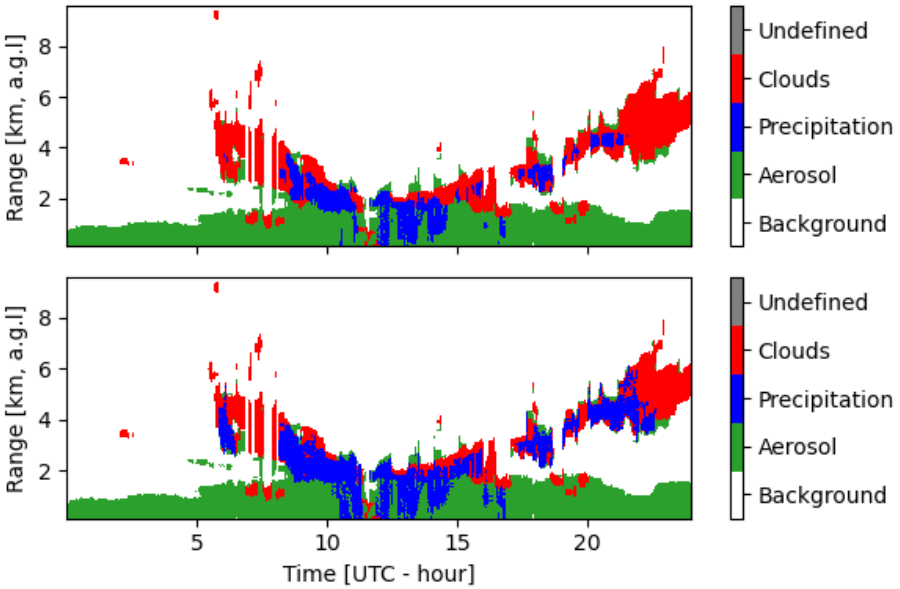

Figure 2.9: Before and after iteration at step 12

in the near range from transportation which resemble clouds. The result is shown in figure 2.10

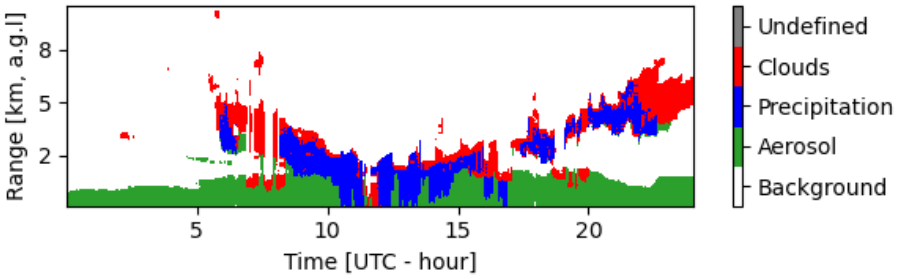

Figure 2.10: Attenuation correction at step 13

Aerosol version 2

14. Fine-tune aerosol class
    (a) Extract aerosol mask from classifier mask
    (b) Perform Density-Based Spatial Clustering of Applications with Noise (DBSCAN) on all data in aerosol mask on time and range dimensions. In addition, record mean velocity and minimum range for each cluster

(c) All clusters have mean velocity less than -0.5 m/s are classified as precipitation

(d) All clusters connect to the ground are classified as aerosol

(e) All clusters have velocity larger than -0.2 m/s are classified as aerosol

(f) All clusters do not satisfy above criteria are classified as undefined

(g) Apply this to the classifier mask

It is observed in the data that some parts of high range ice cloud are not thick enough, and fall down very slowly. This results in some data points misclassified as aerosol. These parts of cloud can be separated as clusters using DBSCAN. By using the average velocity of those clusters, correct classification can be achieved.

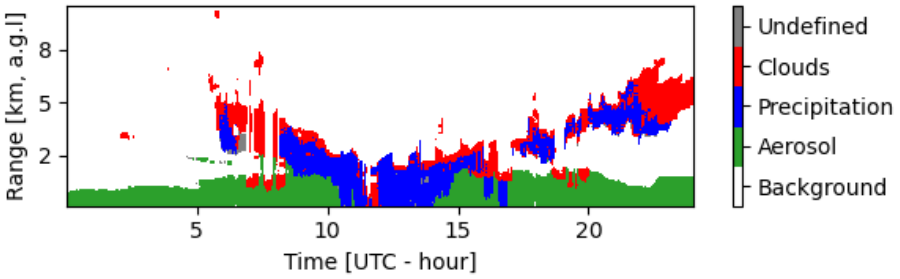

Figure 2.11: Aerosol fine-tune at step 14

Ground precipitation

15. Separate ground precipitation and ice clouds from precipitation class

(a) Extract precipitation mask from classifier mask

(b) Perform Density-Based Spatial Clustering of Applications with Noise (DBSCAN) on all data in precipitation mask on time and range dimensions. In addition, record minimum range for each cluster

(c) All clusters connect to the ground are classified as precipitation

(d) The rest is classified as cloud

(e) Apply this to the classifier mask

This step is simply just to remove falling hydrometers from the clouds and classify them correctly as cloud. The result is shown in figure 2.12.

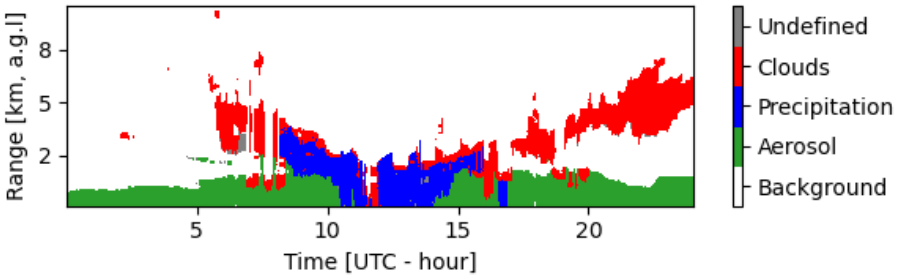

Figure 2.12: Final classification result

2.3.3 Correction for Stream Line XR

As shown in the top of figure 2.13, values of attenuated backscatter in the near range is enhanced. This is due to the high power of the Stream Line XR device and imperfections of the focus function. As the result, the classification algorithm misclassifies those enhanced values as clouds. Hence, correction is needed.

A clear sky in the near range date is selected for Uto-XR instrument (as in figure 2.13), then an averaged attenuated backscatter profile is calculated (log-scaled). Next, the difference between values at range gate 1530 m and all values from the profile from range gate 100 m to 1500 m is calculated and saved as a reference. Finally, all the Uto-XR attenuated backscatter data is log-scaled and subtracted by this reference to obtain the corrected version as in the bottom of figure 2.13. It should be noted that this method is used to fix the attenuated backscatter for the algorithm as it has shown to work satisfactory. A proper correction should be done with modifications of the focus function. However, this is not the aim of this study.

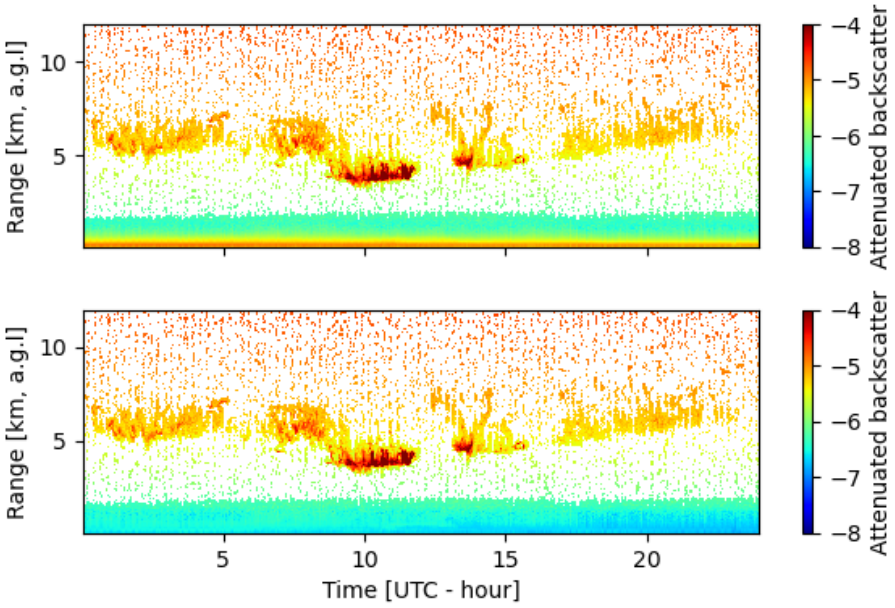

Figure 2.13: Attenuated backscatter original (top) and corrected (bottom) at Uto-32XR 2019-04-05

2.3.4 Evaluation

The algorithm was developed and evaluated using the knowledge gained from the lidar data. However, the effectiveness of the model was not assessed in other experiments or against different models and so the success of the algorithm can only be measured visually not quantifiably.

More results of the classification are shown below in figure 2.14 and 2.15. Beta, velocity and depolarization ratio of the raw data in these figures were filtered with 3 standard deviations of co-SNR to remove noise for clear illustration.

As illustrated in figure 2.14, elevated aerosol layer at 3-4km was detected by the algorithm along with cloud inside that layer. At around 10 UTC, even with negative velocity, the algorithm does not misclassify it with precipitation, and it correctly classifies precipitation at 15 UTC. In addition, clouds from 14 UTC to 22 UTC fluctuate in height significantly, resulting at attenuated signal resembling aerosol signal above cloud levels. Despite that, the algorithm successfully classified those signals as cloud.

In figure 2.15, similar fluctuations of cloud levels can be observed, and the algorithm successfully classified them all as cloud. Likewise, turbulence from 8 UTC to 14 UTC is classified correctly as aerosol despite some negative values

in velocity variable. Moreover, the classification algorithm is able to separate precipitation at 15 UTC to 17 UTC from aerosol.

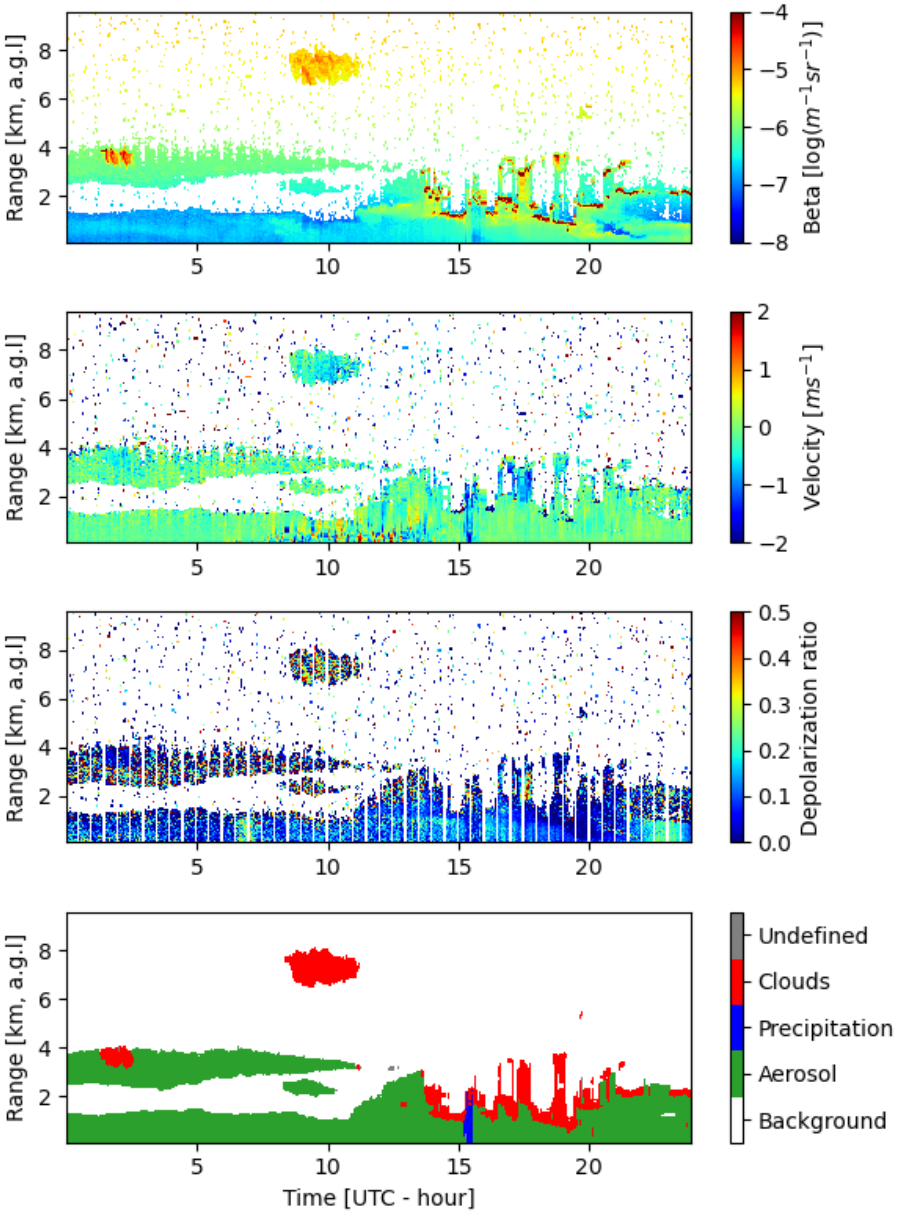

Figure 2.14: Classification result at Hyytiala 2018-04-15

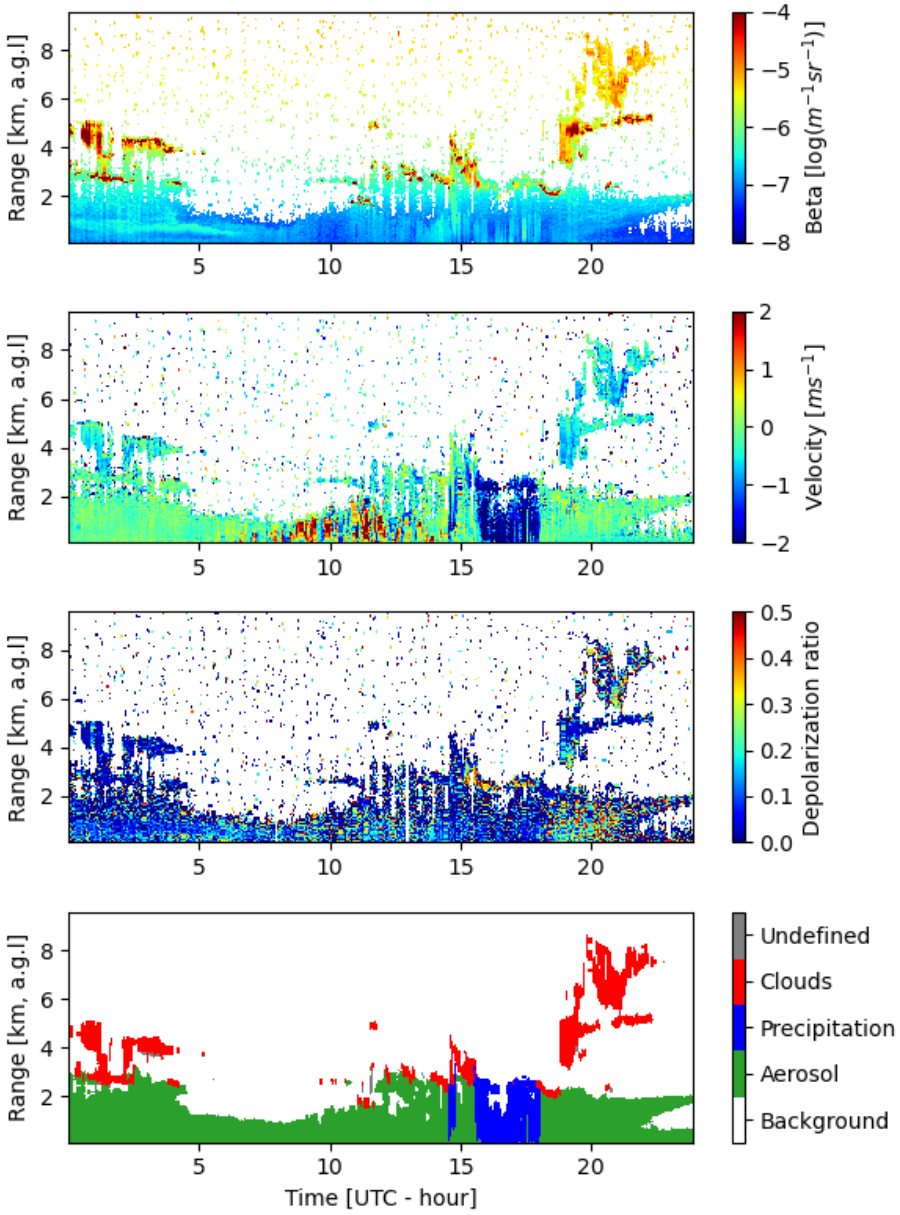

Figure 2.15: Classification result at Hyytiala 2018-06-11

Chapter 3

Results and discussion

3.1 Instrumental stability

3.1.1 Background noise

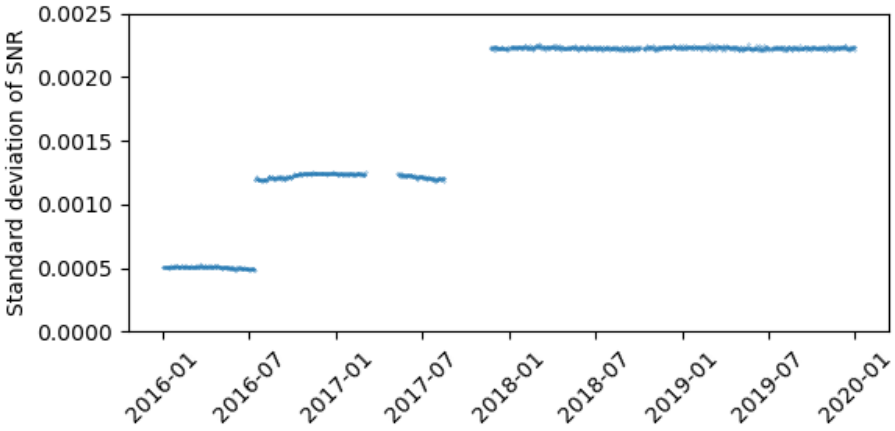

Figure 3.1: Time series of standard deviation of co-SNR in Uto

Period	Integration time
2016-01-01 to 2016-07-12	27.5 seconds
2016-07-13 to 2017-11-22	5 seconds
2017-11-23 to 2019-12-31	2 seconds

Table 3.1: Integration time at Uto

As the co-SNR of the background (i.e cloud-aerosol free region) has a mean of

zero, its standard deviation is used as a measurement for background noise, to indicate instrument deterioration and its effect on the background correction algorithm (Vakkari et al., 2019). Figure 3.1 shows the time series of background noise in instrument 32 and 32XR at Uto. The changes in background noise level are due to different integration time settings(see table 3.1). The higher the integration time, the more observations are averaged, hence the lower the standard deviation of background co-SNR.

Within each level (i.e each integration time setting), background noise is stable, hence no indication of deterioration in this instrument.

3.1.2 Saturation signal at cloud base

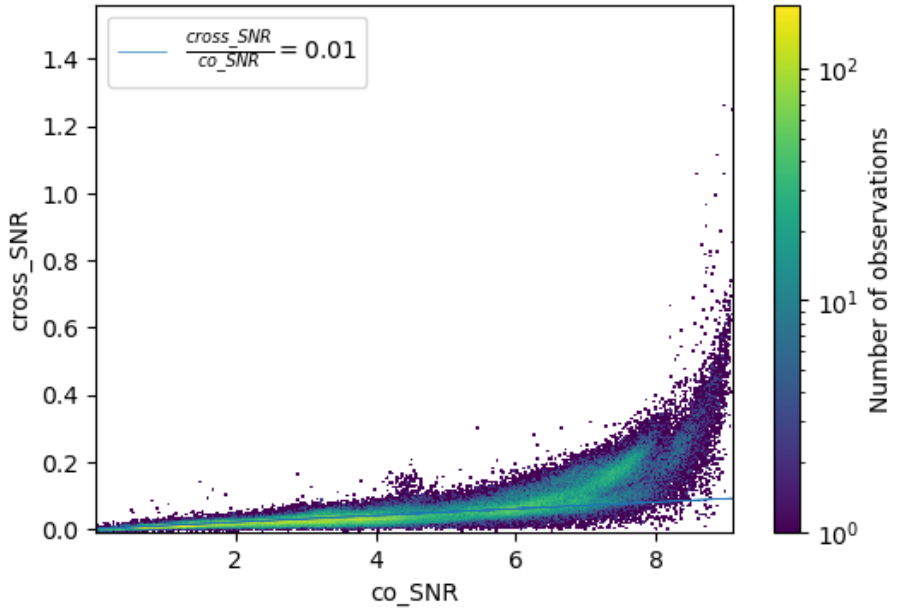

Figure 3.2: 2D histogram of cross-SNR and co-SNR at cloud base, Uto-32XR

Figure 3.2 shows a histogram of co-SNR and cross-SNR of cloud bases. We see an increasing deviation from the linear relationship between co-SNR and cross-SNR as co-SNR gets larger. This indicates saturation of co-polar signal, which results in an increase of depolarization ratio.

Figure 3.3 compare depolarization ratio at cloud base of saturated signals (co-SNR > 6) and unsaturated signals (co-SNR < 6). It is obvious that the distribution of unsaturated signals is thinner and its peak is smaller than of saturated signals, since saturated signals lead to the increase of depolarization ratio.

The solution for this problem is to only keep data with co-SNR less than 6,

where saturation does not occur. However, since the majority of depolarization ratios are not affected, and they only increase during saturation, this problem does not interfere with the determination of bleed through as only the peak of smaller depolarization ratio distribution is taken into account.

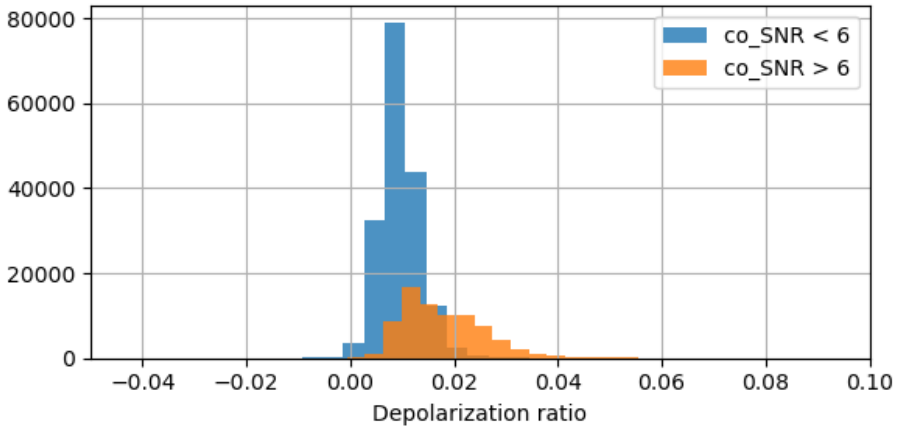

Figure 3.3: Saturation signals in histogram of depolarization ratio at cloud base in Uto-32XR

3.1.3 Depolarization ratio at cloud base

All depolarization ratios at cloud base in Uto are collected and shown as histograms in figure 3.4 and 3.6 and time series in Figure 3.5 and 3.7. For the instrument 32XR, depolarization ratio is high during winter while low in the summer. This might be due to the frequent occurrences of mixed phase cloud in the winter, though has not been verified by other methods. On the other hand, for instrument 32, high depolarization ratio can be seen frequently in both winter and summer. Beside the contribution of mixed phase clouds, high integration time also can be the reason for this high depolarization ratio.

As mentioned previously, in order to determine the bleed through of the instruments, the lowest peak of the histogram is used. The result of the bleed through is shown in table 3.2.

Bleed through was determined similarly for all other instruments (Hannah Lobo, Finnish Meteorological Institute, personal communication, 13 August 2020). The result (table 3.2) was used for to correct depolarization ratio for bleed through in this study.

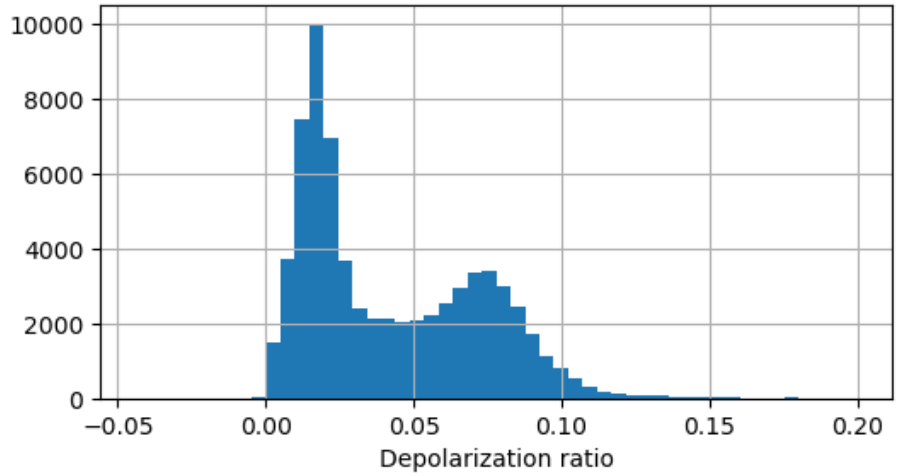

Figure 3.4: Histogram of depolarization ratio at cloud base for Uto-32

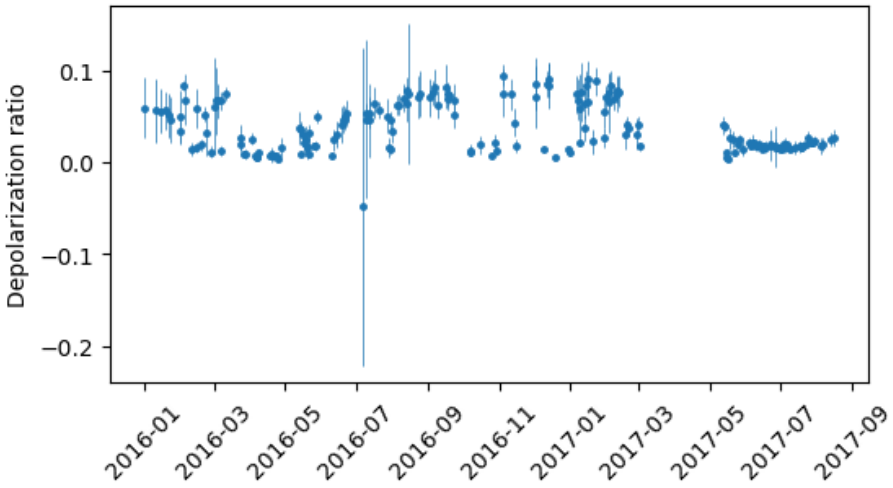

Figure 3.5: Time-series of depolarization ratio at cloud base for Uto-32

Source	**Instrument**	**Mean**	**Standard deviation**
This study	Uto-32	0.017	0.0072
	Uto-32XR	0.0121	0.0071
Hannah Lobo.	Hyytiälä-33	0.0187	0.0165
Finnish Meteorological Institute	Hyytiälä-46	0.0164	0.0105
personal communication	Kuopio-53	0.0134	0.0079
13 August 2020	Sodankylä-54	0.0092	0.0055

Table 3.2: Mean and standard deviation of bleed through of all the instruments

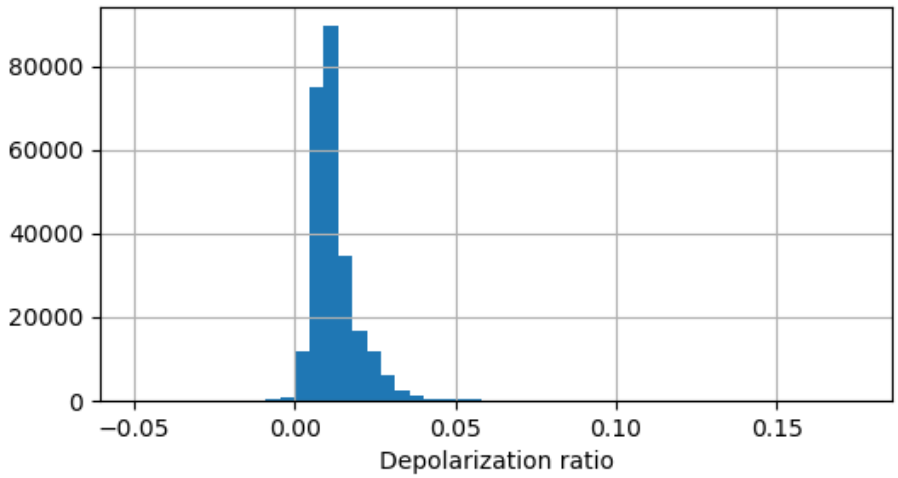

Figure 3.6: Histogram of depolarization ratio at cloud base for Uto-32XR

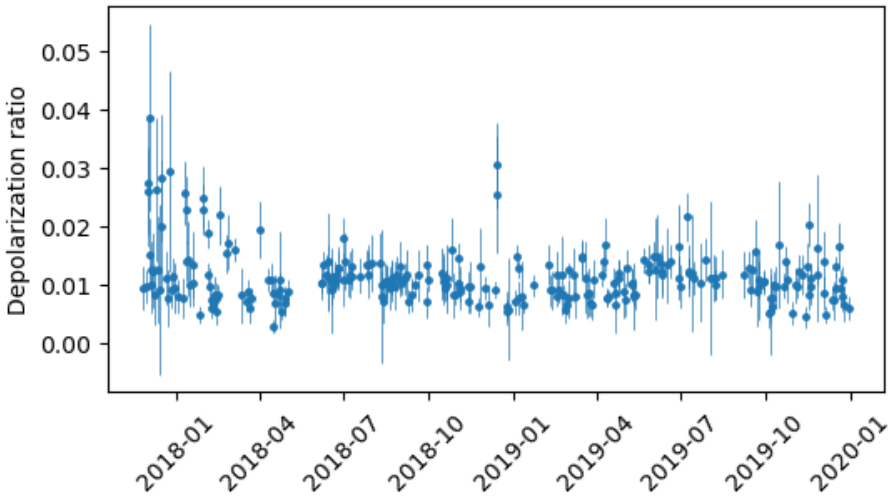

Figure 3.7: Time-series of depolarization ratio at cloud base for Uto-32XR

3.2 Aerosol depolarization ratio

With the classification algorithm, aerosol masks from the original data can be obtained. However, since aerosol signals are relatively weak, additional averaging is needed to reduce instrumental noise. The averaging process is done by first binning the data by 300m and 1 hour. Then all aerosol data points in each bin are averaged, followed by the calculation of depolarization ratio. If less than 50 percent of data points in a bin are classified as aerosol by the algorithm, that bin is ignored. The following statistics are calculated on this averaged data.

3.2.1 Seasonal

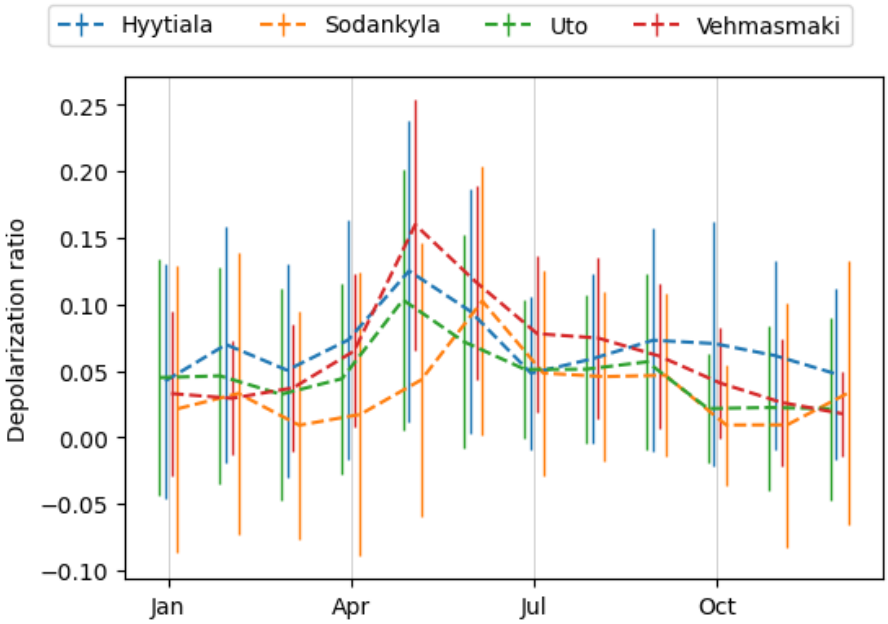

Figure 3.8: Averaged monthly mean and standard deviation of depolarization ratio in each site over the whole study period

Figure 3.8 shows averaged monthly mean and standard deviation of depolarization ratio in all sites. The peaks in mean depolarization ratio coincide with intense pollination periods (Bohlmann et al., 2019). While Hyytiala, Uto and Vehmasmaki start their elevated depolarization ratio period on May, Sodankyla, which located in the highest latitude, has its elevated depolarization ratio period began on June. After the peaks, mean depolarization ratios decrease steadily in summer months from July to September. During the winter from Oct to April, mean depolarization ratios stay the lowest below 0.05.

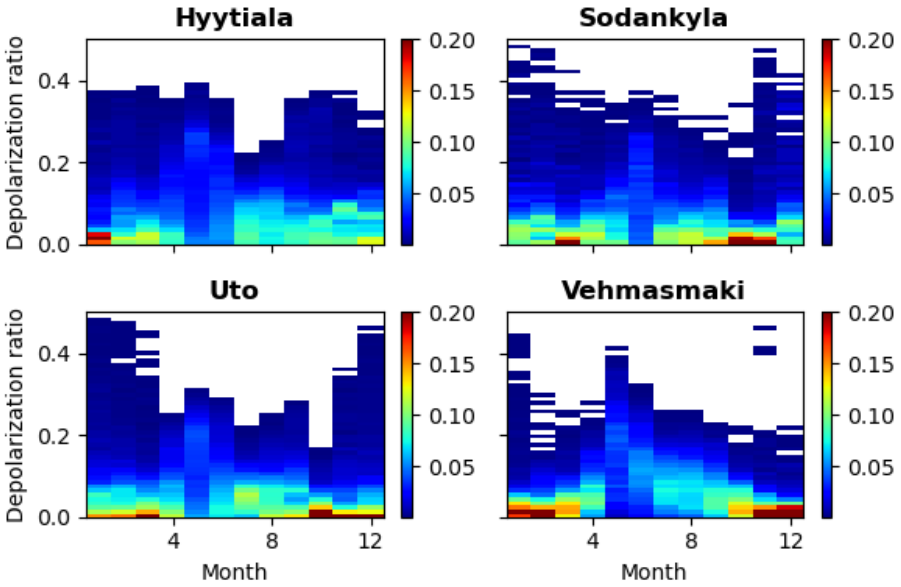

Figure 3.9: 2D histogram of aerosol depolarization ratio distribution each month in all sites in the whole study period. Color bar is fraction of observations in each month, all values in each month add up to 1

These elevated depolarization ratio periods can also be seen clearly in figure 3.9, where depolarization ratio distribution of each month is shown across all the sites. During these periods, the spread of aerosol depolarization ratio distribution is larger, indicating multiple aerosol types existing simultaneously. Located in forest areas, Hyytiala and Vehmasmaki have elevated depolarization ratio periods which lasted up to two months from May to June comparing to only one month in Sodankyla and Uto. It should be noted that Uto is a small island located in the Baltic sea, so this elevated depolarization ratio aerosol in Uto is probably transported pollen from land.

From figure 3.8 and figure 3.9, seasonality of depolarization ratio can be divided into the following periods:

- October to April: during this late autumn to early spring months, depolarization ratio across all sites stay at the lowest.

- May: this is the start of elevated depolarization ratio period in Uto, Hyytiala and Vehmasmaki.

- June: this is the start the of elevated depolarization ratio period in Sodankyla.

- July to September: Elevated depolarization ratio aerosols can be found during

this period. Their depolarization ratio is larger than from October to April, but not as high as in May and June.

Statistics of overall and seasonal depolarization ratios are shown in table 3.3.

Hyytiala has a higher mean depolarization ratio compared to other sites from October to April, while Vehmasmaki has the highest mean depolarization ratio in summer months May and June. On the other hand, mean depolarization ratio in Sodankyla remains the lowest through out the year, except in June when its elevated depolarization ratio period starts.

Location	**Oct-Apr**	**May**	**June**	**Jul-Sep**	**Overall**
Uto	0.035±0.073	0.103±0.098	0.072±0.080	0.052± 0.057	0.055±0.076
Hyytiala	0.063±0.086	0.125±0.113	0.095±0.092	0.057± 0.067	0.076±0.090
Vehmasmaki	0.038±0.0.051	0.160±0.094	0.117±0.073	0.073± 0.059	0.076±0.071
Sodankyla	0.015±0.091	0.043±0.103	0.102±0.101	0.047± 0.068	0.041±0.089

Table 3.3: Mean and standard deviation of depolarization ratio at 1565nm across all sites during the study period

Interannual changes in aerosol depolarization ratio seasonality can be found in figures 3.10, 3.11, 3.12 and 3.13. One common characteristic from these plots is that much more aerosol occurred in spring-summer months from May to September compared to the rest of the year. As a result, statistics during this period are more reliable.

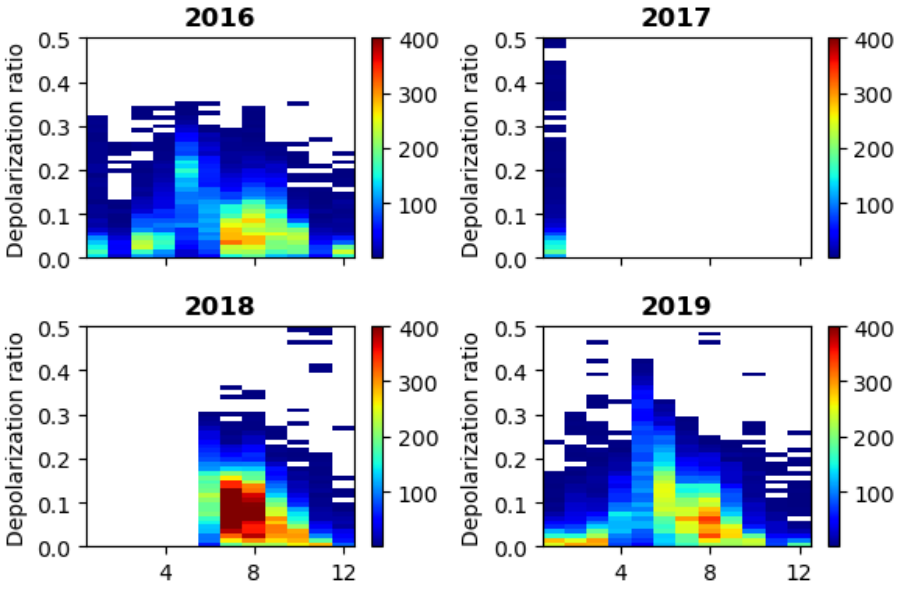

Figure 3.10: 2D histogram of aerosol depolarization ratio each month in Vehmasmaki. The color bar is number of observations

Figure 3.10 describes the variability across multiple years of aerosol depolarization ratio seasonality in Vehmasmaki. There is a lot of missing data especially in 2017 in Vehmasmaki. Compared to 2019 and 2016, there is much more aerosol in July and August 2018. As will be shown later, this unusual high amount of aerosol in 2018 can also be seen in other sites.

During May 2016, there is a clear population of depolarization ratio at around 0.2 indicating pollen (Bohlmann et al., 2019). Although in April and May 2019, no clear peak of depolarization ratio can be found, this spread of aerosol distribution suggests a mixture of aerosol types with both high and low depolarization ratio. This is an indication of the elevated depolarization ratio period which starts early in April 2019 comparing to other years in May.

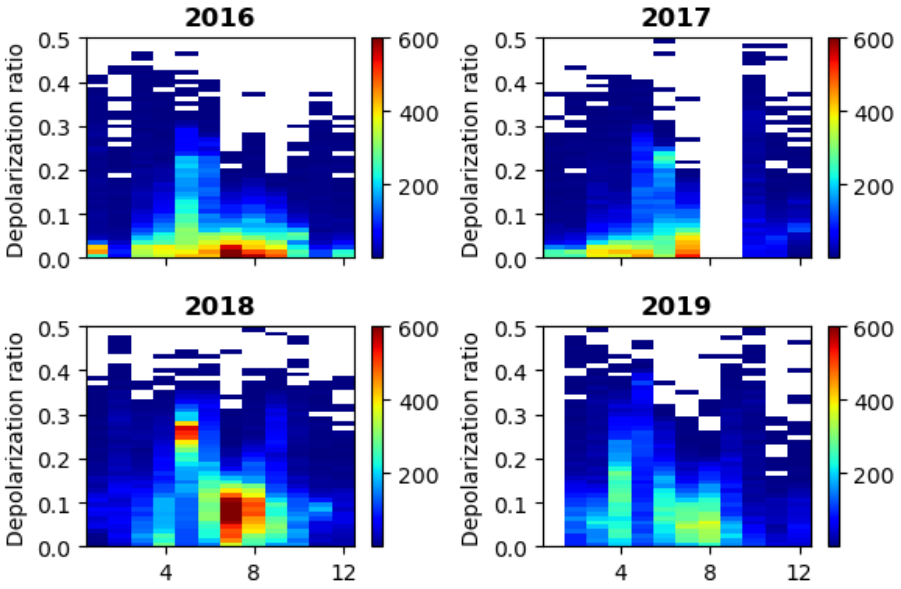

Figure 3.11: 2D histogram of aerosol depolarization ratio each month in Hyytiala, color bar is number of observations

In Hyytiala, the pattern of interannual changes in aerosol depolarization ratio is demonstrated in figure 3.11. Little to no aerosol can be observed in the winter from October to April with the majority of depolarization ratios less than 0.05.

Similar to Vehmasmaki, high amount of aerosol with depolarization ratio around 0.1 can be observed in July and August 2018. The intense pollination period in Hyytiala can be observed by the spread of depolarization ratio from May in 2016, 2017 and 2019, and by a high depolarization ratio population of around 0.25 in May 2018. In addition, in 2019, Hyytiala's elevated depolarization ratio period started early in April compared to other years in May.

On the other hand, the spread of depolarization ratio distribution during June - August of 2018 and 2019 is much larger than in 2016 and 2017. Though more studies are needed to explain this, it shows that there are more aerosols with high depolarization ratio in that period of 2018 and 2019 compared to 2016 and 2017.

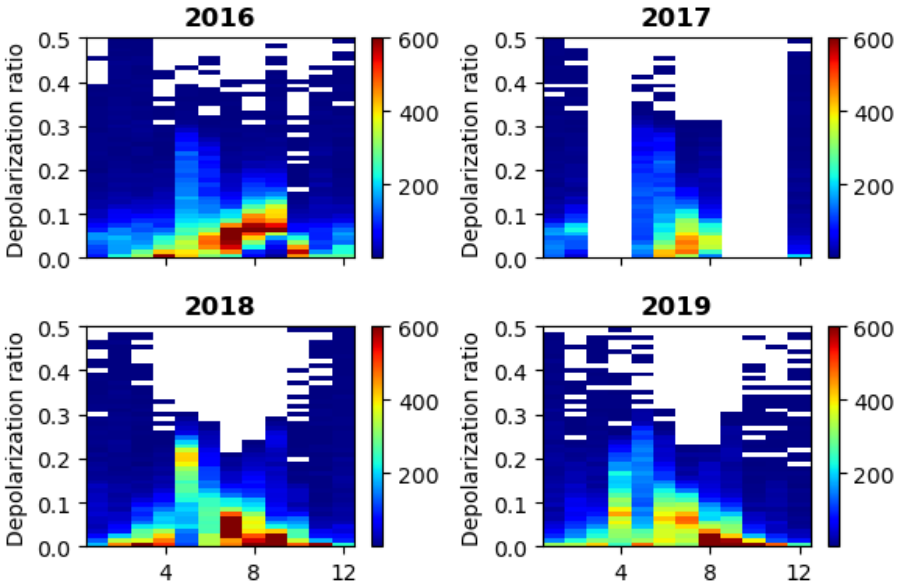

Figure 3.12: 2D histogram of aerosol depolarization ratio each month in Uto. The color bar is number of observations

In Uto, interannual changes in aerosol depolarization ratio seasonality can be derived in figure 3.12. Similarly to other sites, Uto has very little aerosol with a low depolarization ratio less than 0.05 during the winter period from November to March.

The intense pollination period in Uto can be observed by the spread of depolarization ratio from May 2016, 2017 and 2019, and by a high depolarization ratio population of around 0.25 in May 2018. This high depolarization ratio was also observed in Hyytila, which indicates that the similar pollen was transported to Uto. In addition, in 2019, Uto's intense pollination period starts early in April comparing to other years in May.

In 2016, in contrast to other years, there is an increase in depolarization ratio value from June to September, then a sharp drop to around 0.05 in October. This unusual increase can indicate the presence of high depolarization ratio aerosol such as transported forest fire dust, dust mixed with inspherical particles. More studies are needed to explain this phenomenon as this increasing trend can only be observed in Uto.

Similarly to Vehmasmaki and Hyytiala, there was a lot more aerosol during July in Uto in 2018 compared to 2017 and 2019. These aerosol also have depolarization ratios of around 0.05 which is less than the depolarization ratios in Vehmasmaki and Hyytiala at the same time.

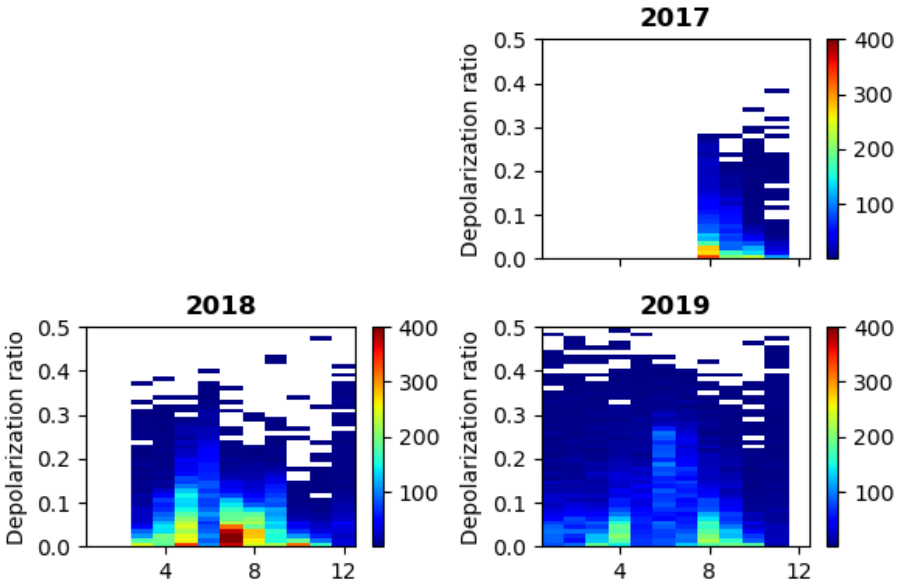

Figure 3.13: 2D histogram of aerosol depolarization ratio each month in Sodankyla. The color bar is number of observations.

In Sodankyla, the pattern of its interannual changes in aerosol depolarization ratio is shown in fig 3.13. There is a lot of missing data in this site and one common pattern across all the years is that there is little to no aerosol can be observed in the winter from October to February with a depolarization ratio less than 0.05.

In 2018, the elevated depolarization ratio period can be observed as early as in May due to the high spread of depolarization ratio. Also in this year, much higher amount of aerosol is observed during July than in 2019, just like in other sites. In addition, in 2019, aerosol with an elevated depolarization ratio starts to appear later in June.

3.2.2 Spectral dependency

Figure 3.14 illustrates mean and standard deviation of depolarization ratio of different aerosol types at multiple wavelengths of 355 nm, 532 nm, 710 nm, 1064 nm and 1565 nm in literature. Spectral dependency of aerosol depolarization ratio can be observed in certain aerosol types, and can vary across multiple studies. For example, Saharan dust depolarization ratio increases with wavelength in Vakkari et al. (2020), while decreases in Freudenthaler et al. (2009), but appearing to have no relation with wavelength in Haarig et al. (2017) and Burton et al. (2015). Depolarization ratio of smoke has a negative dependency on wavelength; the higher the wavelength, the smaller the depolarization ra-

tio.

The last subplot in figure 3.14 displays the overall mean depolarization ratio and its standard deviation at 1565nm, across all the sites. It should be noted that mean aerosol depolarization ratio statistics in this study are averaged across the whole study period, so their statistics include all types of aerosol. In contrast, other studies usually report data in just a short period of time, with only a certain type of aerosol.

Compared to dust, pollen and ash, overall mean depolarization ratios across all the sites in this study are smaller. During the intense pollination period of May, April or June (see table 3.3), mean depolarization ratios are similar to the depolarization ratio of pollen found in Bohlmann et al. (2019) and Vakkari et al. (2020). Depolarization ratios of marine aerosol in Vakkari et al. (2020) and Groß et al. (2011) are found to be similar to mean depolarization ratio in Uto from April to October (see table 3.3).

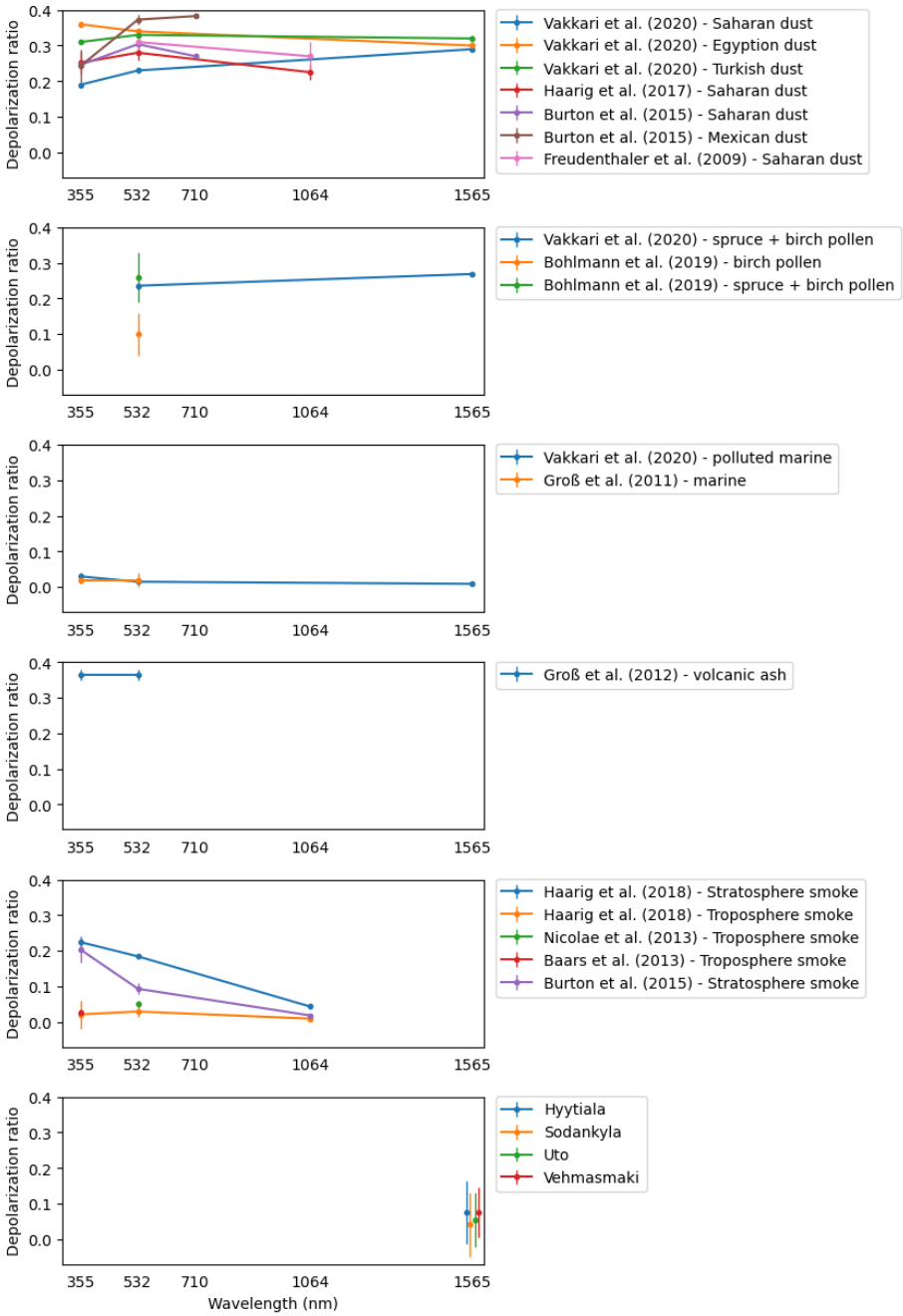

Figure 3.14: Wavelength dependency of depolarization ratio in literature (table 5.1) categorized by aerosol type at 355 nm, 532 nm, 710 nm, 1064 nm and 1565 nm and this study (table 3.3) at 1565 nm.

3.2.3 Diurnal cycles

Figure 3.15 illustrates the distribution of mean depolarization ratio every hour for each month across all sites. The common theme of these plots is that aerosol with high depolarization ratio occurs mostly in May and June. In this period, mean depolarization ratio in Hyytiala and Vehmasmaki peaks at noon. This suggests high pollen concentration in these sites. In the rest of the year, the same pattern of high depolarization ratio at noon can be observed in Vehmasmaki but not in Hyytiala, Uto or Sodankyla.

In Sodankyla, although most aerosol is present in the summer, the night time is short during this period due to its location inside the Arctic circle. Hence, the effect of the diurnal cycle is minimal. While in Uto, aerosol with high depolarization ratio during summer peaks at night and remain low during the day. The high value at night might be due to transported pollen arriving from land.

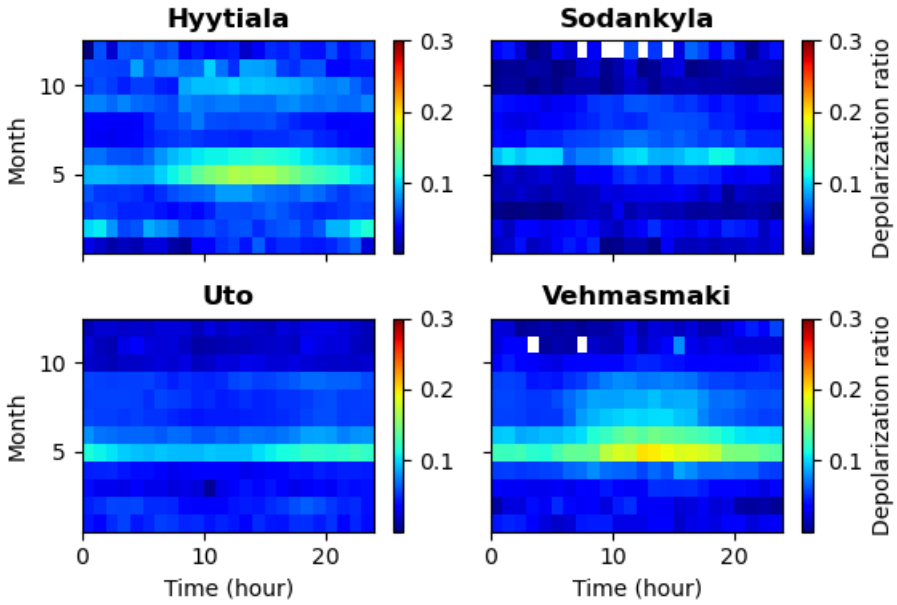

Figure 3.15: Mean of aerosol depolarization ratio in each hour each month across all locations

3.2.4 Range and relative humidity

Figure 3.16 describes the relationship of depolarization ratio and range across all sites in the study period. Table 3.4 shows parameters of these correlations, which are fitted using linear regression.

Although all correlations are statistically significant, their R-squared values

(Pearson correlation) explain more about the strength of these correlations. From January to March and October to December, all R-squared values are low, describing negligible correlation between range and depolarization ratio in this period. From April to June, there are strong correlations in Uto, Hyytiala and Vehmasmaki. With each kilometer increase in range, depolarization ratio decreases by 0.051 in Uto, 0.042 in Hyytiala and 0.05 in Vehmasmaki. On the other hand, minimal correlation is found in Sodankyla. This can be explained by looking at figure 3.16, which shows that there is an increasing trend of depolarization ratio with range below 600 m. However, it decreases after this range in Sodankyla from April to June. From July to September, strong correlations are found in all sites, with each kilometer increase in range, depolarization ratio decreases by 0.023 in Uto, 0.03 in Vehmasmaki and 0.078 in Sodankyla.

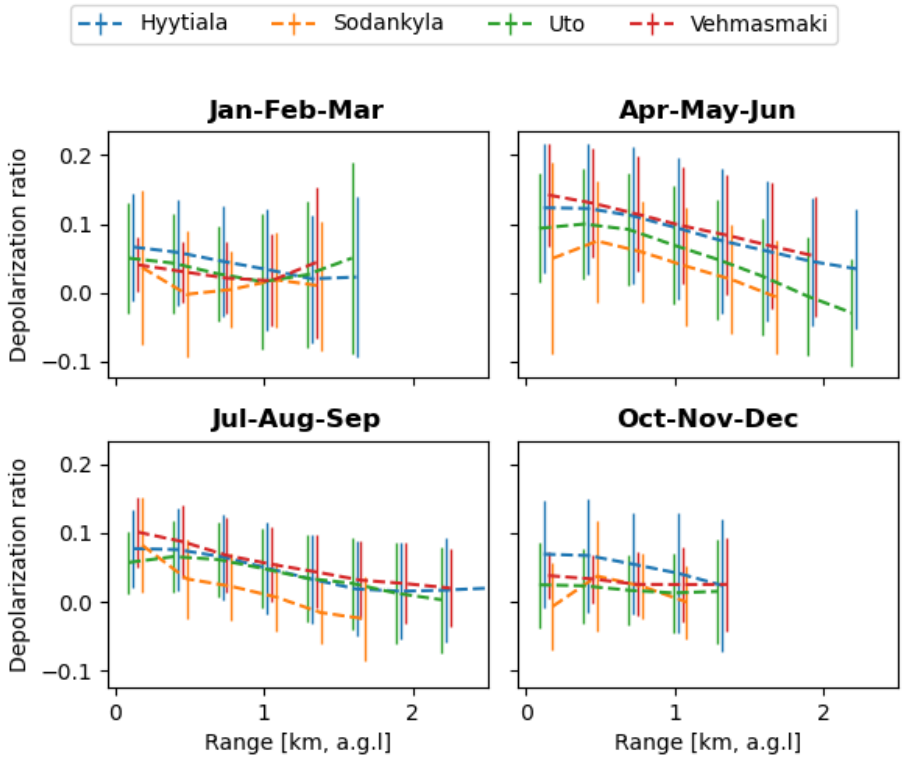

Figure 3.16: Depolarization ratio vs range in all locations. All data is used, range is binned every 300m

Period	**Location**	**Slope**	**p-value**	**R-squared**
Jan-Mar	Uto	-0.008	$< 1e-5$	0.001
	Hyytiala	-0.01	$< 1e-5$	0.003
	Vehmasmaki	0.009	$< 1e-5$	0.004
	Sodankyla	-0.018	$< 1e-5$	0.003
Apr-Jun	Uto	-0.051	$< 1e-5$	0.107
	Hyytiala	-0.042	$< 1e-5$	0.065
	Vehmasmaki	-0.05	$< 1e-5$	0.081
	Sodankyla	-0.024	$< 1e-5$	0.008
Jul-Sep	Uto	-0.023	$< 1e-5$	0.047
	Hyytiala	-0.03	$< 1e-5$	0.087
	Vehmasmaki	-0.041	$< 1e-5$	0.157
	Sodankyla	-0.078	$< 1e-5$	0.184
Oct-Dec	Uto	-0.01	$< 1e-5$	0.003
	Hyytiala	-0.018	$< 1e-5$	0.006
	Vehmasmaki	-0.011	$< 1e-5$	0.008
	Sodankyla	0.043	$< 1e-5$	0.027

Table 3.4: Linear regression analysis summary for Range [km] predicting Depolarization ratio in each period for every location.

One of the most significant factors that impacts aerosol's physical properties is relative humidity. Studies show that the size and shape of pollen grains are affected by relative humidity (Franchi, Pacini, & Rottoli, 1984; Griffiths et al., 2012; Katifori, Alben, Cerda, Nelson, & Dumais, 2010), as it determines if aerosol particles will grow or shrink through a process called hygroscopic growth. The result is that different optical properties can be observed at different relative humidity, such as significantly higher depolarization of the backscattered light.

Figure 3.17 shows the correlation between depolarization ratio and relative humidity. Table 3.5 shows parameters of these correlations, which are fitted using linear regression. It is noteworthy that in figure 3.17, all values within each 10% relative humidity bin have been averaged to show trends, but the number of observations within each bin is not shown. However, for the statistical tests used to calculate the correlations, the data has not been averaged. In addition, only depolarization ratios below 300 m are taken for these correlations.

All correlations with p-value larger than 1e-5 are non-reliable, as explained by

their 0 R-squared values. From April to June, negative correlations between relative humidity and depolarization ratio can be observed across all sites. With each percentage increase in relative humidity, depolarization ratio decreases by 0.001 in Uto, 0.002 in Hyytiala, 0.002 in Vehmasmaki and 0.001 in Sodankyla. Similar negative correlation can be found in Vehmasmaki from July to September. In other periods, the relationship between depolarization ratio and relative humidity is negligible due to either small slope, large p-value or low R-squared values.

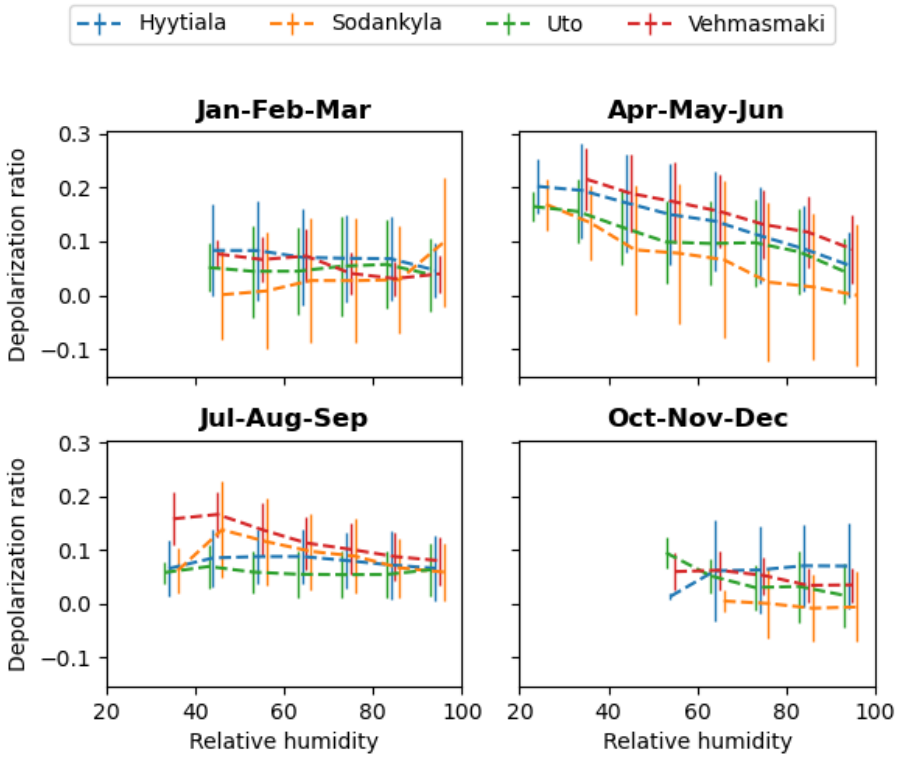

Figure 3.17: Depolarization ratio vs relative humidity in all locations. All data is used, relative humidity is binned every 10%.

Period	Location	Slope	p-value	R-squared
Jan-Mar	Uto	-0.0001	0.07457	0.0
	Hyytiala	-0.0005	$< 1e-5$	0.004
	Vehmasmaki	-0.0003	$< 1e-5$	0.003
	Sodankyla	-0.00	0.82596	0.0
Apr-Jun	Uto	-0.0011	$< 1e-5$	0.038
	Hyytiala	-0.0021	$< 1e-5$	0.104
	Vehmasmaki	-0.002	$< 1e-5$	0.117
	Sodankyla	-0.0009	$< 1e-5$	0.018
Jul-Sep	Uto	0.0003	$< 1e-5$	0.004
	Hyytiala	-0.0005	$< 1e-5$	0.011
	Vehmasmaki	-0.0013	$< 1e-5$	0.1
	Sodankyla	-0.0006	$< 1e-5$	0.015
Oct-Dec	Uto	-0.0014	$< 1e-5$	0.018
	Hyytiala	0.0006	$< 1e-5$	0.002
	Vehmasmaki	-0.0005	$< 1e-5$	0.006
	Sodankyla	0.0003	0.07361	0.0

Table 3.5: Linear regression analysis summary for relative humidity predicting depolarization ratio in each period for every location.

The negative correlation between depolarization ratio and relative humidity can be explained by hygroscopic growth, during which aerosol particles become more spherical as relative humidity increases. A study by Haarig et al. (2017) in Barbados also found a similar correlation; they found that a dust layer has a higher depolarization ratio located on top of a moist marine aerosol layer with lower depolarization ratio but higher humidity. However, Bohlmann et al. (2019) analyze only pollen in May at Vehmasmaki and found no correlation between relative humidity and depolarization ratio at wavelength 532nm.

The negative correlation between depolarization ratio and range in the summer can be explained by a higher amount and more types of aerosol. Pollen usually has a high depolarization ratio and a large particle size. Hence, it is more concentrated near the ground due to gravitational force, resulting in higher depolarization ratio in the near range. In addition, the increase of relative humidity with range also can also be a contributing factor to this.

In summary, correlation between depolarization with range and relative humidity can both be observed in the summer with the abundance of pollen from April

to June. Two processes that might contribute to this correlation are gravitational settling and hygroscopic growth. With limited data, it is not possible to conclude which process plays a larger role. On the other hand, in the winter, there is no non-spherical aerosol to begin with. Hence, any effect by range or relative humidity to depolarization ratio of aerosol is minimal.

Chapter 4

Conclusions

In this study, the use of Halo Doppler lidars for long-term monitoring of aerosol particle depolarization ratio was investigated. The first aim was to investigate the stability of the instrument noise level and polarizer performance. The second aim was to generate statistics of aerosol particle linear depolarization ratio at different site in Finland.

The stability of the noise level was investigated by assessing the co-SNR time series of the background areas (see Section 3.1.1). It is found that within each integration time setting, the noise level is stable for the Utö instruments. Data in Kumpula was poor quality, so its instrument is excluded in all analysis of this study.

The bleed through of the polarizer was calculated through depolarization ratio at liquid cloud base (see Section 3.1.3). It is found that value of the bleed through is 0.017 $\pm$ 0.0072 in Uto-32 and 0.0121 $\pm$ 0.0071 in Uto-32XR. This bleed through was used to correct depolarization ratio values of Halo Doppler lidar.

In order to analyse aerosol particle depolarization ratio an algorithm was developed to distinguish aerosol particles from clouds and precipitation (see Section 2.3). In the course of the algorithm development, an unexpected increase in near-range beta was observed for Uto-32XR lidar, but not for other lidars. This issue was attributed to the imperfect focus function and was accounted for (see Section. 3.1.2). However, more studies are needed to better understand this problem. The classification compares well with visual inspection as shown in figures 2.14 and 2.15.

The classification algorithm was found to be successful at extracting aerosol data from the instruments. From the statistics of aerosol depolarization ratio (see Section 3.2.1), it is found that aerosol depolarization ratio varies across all the sites Finland throughout the whole study period. Overall, depolarization

ratios are at 0.055 ± 0.076 in Uto, 0.076 ± 0.090 in Hyytiala, 0.076 ± 0.071 in Vehmasmaki and 0.041 ± 0.089 in Sodankyla. All these sites have low depolarization ratios in the winter months and high depolarization ratios in the summer months up to (0.15) which is probably due to pollen particles. In May 2018, unusual high depolarization ratios were observed up to 0.2 for Uto and 0.3 for Hyytiala compared other years. Sodankyla, which is located near the Arctic, usually has aerosols with lower depolarization ratios than other sites.

Diurnal patterns of depolarization ratio varies across all sites (see Section 3.2.3). In the elevated depolarization ratio period (May-June), depolarization ratio is lowest in the middle of the day for Uto, but highest for Hyytiala and Vehmasmaki. During the night in this period, depolarization ratio in Uto increases compared to daytime ratios, which can be attributed to transported pollen. No clear impact of diurnal cycles in Sodankyla is found due to short nighttime hours in this period.

From April to June across all the sites, depolarization ratio was found to decrease with height (see Section 3.2.4). At the same time, depolarization ratio was found to decrease with increasing relative humidity. With limited measurements, no clear conclusions can be drawn as to which process plays a more important role.

In conclusion, long-term performance of Halo Doppler lidars (excluding one in Kumpula) was found to be satisfactory for the determination of aerosol depolarization ratio. This extends the capabilities of the Finnish remote sensing network (Hirsikko et al., 2014) to identify non-spherical aerosol particles, which is important for the security of supply in Finland in the case of a volcanic eruption.

Chapter 5

Appendix

Study	Description	Depolarization ratio 355nm	532nm	710nm	1064nm	1565nm
Vakkari et al. (2020)	Limassol April 2017 Saharan dust	0.19±0.008	0.23±0.008			0.29±0.008
	Limassol April 2017 Egyption dust	0.36±0.01	0.34±0.002			0.30±0.005
	Limassol April 2017 Turkish dust	0.31±0.006	0.33±0.005			0.32±0.008
Haarig et al. (2017)	Barbados 2013-2014 Saharan dust	0.252±0.030	0.280±0.020		0.225±0.022	
Burton et al. (2015)	US July 2014 Saharan dust	0.246±0.018	0.304±0.005	0.270±0.005		
	Mexico Chihuahua Feb 2013 local dust	0.243±0.046	0.373±0.014	0.383±0.006		
Groß et al. (2011)	Cape Verde 2008 Saharan dust	0.24 – 0.27	0.29 – 0.31	0.36 – 0.40		
Freudenthaler et al. (2009)	Morocco May-June 2006 Saharan dust		0.31±0.03		0.27± 0.04	
Groß et al. (2011)	Cape Verde 2008 marine	0.02±0.01	0.02±0.02			
Vakkari et al. (2020)	Cyprus Limassol May 2017 polluted marine	0.03±0.01	0.015±0.002			0.009±0.003
Vakkari et al. (2020)	Finland Vehmasmäki May 2016 spruce + birch pollen		0.236±0.009			0.269±0.005
Bohlmann et al. (2019)	Finland Vehmasmäki May 2016 birch pollen		0.10±0.06			
	Finland Vehmasmäki May 2016 spruce + birch pollen		0.26±0.07			
Groß et al. (2012)	Germany Maisach April 2010 volcanic ash	0.35-0.38	0.35-0.38			

Table 5.1: Mean and standard deviation of depolarization ratio in literature at different wavelengths

References

Aarnio, P., Yli-Tuomi, T., Kousa, A., Mäkelä, T., Hirsikko, A., Hämeri, K., ... Jantunen, M. (2005). The concentrations and composition of and exposure to fine particles (PM2.5) in the Helsinki subway system. *Atmospheric Environment*, *39*(28), 5059–5066. doi:10.1016/j.atmosenv.2005.05.012

Albersheim, S., & Guffanti, M. (2009). The United States national volcanic ash operations plan for aviation. In *Natural hazards* (Vol. 51). doi:10.1007/s11069-008-9247-1

Alexander, D. (2013). Volcanic ash in the atmosphere and risks for civil aviation: A study in European crisis management. *International Journal of Disaster Risk Science*, *4*(1). doi:10.1007/s13753-013-0003-0

Al-Saadi, J., Szykman, J., Pierce, R. B., Kittaka, C., Neil, D., Chu, D. A., ... Fishman, J. (2005). Improving National Air Quality Forecasts with Satellite Aerosol Observations. *Bulletin of the American Meteorological Society*, *86*(9), 1249–1262. doi:10.1175/BAMS-86-9-1249

Baars, H., Ansmann, A., Althausen, D., Engelmann, R., Artaxo, P., Pauliquevis, T., & Souza, R. (2011). Further evidence for significant smoke transport from Africa to Amazonia. *Geophysical Research Letters*, *38*(20). doi:10.1029/2011GL049200

Baars, H., Ansmann, A., Althausen, D., Engelmann, R., Heese, B., Mller, D., ... Souza, R. (2012). Aerosol profiling with lidar in the Amazon Basin during the wet and dry season. *Journal of Geophysical Research Atmospheres*, *117*(21). doi:10.1029/2012JD018338

Baars, H., Kanitz, T., Engelmann, R., Althausen, D., Heese, B., Komppula, M., ... Zamorano, F. (2016). An overview of the first decade of PollyNET: An emerging network of automated Raman-polarization lidars for continuous aerosol profiling. *Atmospheric Chemistry and Physics*, *16*(8), 5111–5137. doi:10.5194/acp-16-5111-2016

Baars, H., Seifert, P., Engelmann, R., & Wandinger, U. (2017). Target categorization of aerosol and clouds by continuous multiwavelength-polarization lidar measurements. *Atmospheric Measurement Techniques*, *10*(9), 3175–3201. doi:10.5194/amt-10-3175-2017

Bohlmann, S., Shang, X., Giannakaki, E., Filioglou, M., Saarto, A., Romakkaniemi, S., & Komppula, M. (2019). Detection and characterization of birch pollen in the atmosphere using a multiwavelength Raman

polarization lidar and Hirst-type pollen sampler in Finland. *Atmospheric Chemistry and Physics*, *19*(23). doi:10.5194/acp-19-14559-2019

Bolić, T., & Sivčev, Ž. (2011). Eruption of Eyjafjallajökull in Iceland: Experience of European air traffic management. *Transportation Research Record*(2214). doi:10.3141/2214-17

Bond, T. C., Doherty, S. J., Fahey, D. W., Forster, P. M., Berntsen, T., DeAngelo, B. J., ... Zender, C. S. (2013). Bounding the role of black carbon in the climate system: A scientific assessment. *Journal of Geophysical Research: Atmospheres*, *118*(11), 5380–5552. doi:https://doi.org/10.1002/jgrd.50171

Boulon, J., Sellegri, K., Hervo, M., & Laj, P. (2011). Observations of nucleation of new particles in a volcanic plume. *Proceedings of the National Academy of Sciences of the United States of America*, *108*(30). doi:10.1073/pnas.1104923108

Burton, S. P., Ferrare, R. A., Hostetler, C. A., Hair, J. W., Rogers, R. R., Obland, M. D., ... Froyd, K. D. (2012). Aerosol classification using airborne High Spectral Resolution Lidar measurements-methodology and examples. *Atmospheric Measurement Techniques*, *5*(1). doi:10.5194/amt-5-73-2012

Burton, S. P., Hair, J. W., Kahnert, M., Ferrare, R. A., Hostetler, C. A., Cook, A. L., ... Rogers, R. R. (2015). Observations of the spectral dependence of linear particle depolarization ratio of aerosols using NASA Langley airborne High Spectral Resolution Lidar. *Atmospheric Chemistry and Physics*, *15*(23). doi:10.5194/acp-15-13453-2015

Durant, A. J., Villarosa, G., Rose, W. I., Delmelle, P., Prata, A. J., & Viramonte, J. G. (2012). Long-range volcanic ash transport and fallout during the 2008 eruption of Chaitén volcano, Chile. *Physics and Chemistry of the Earth*, *45-46*. doi:10.1016/j.pce.2011.09.004

Eliasson, J., Watson, I. M., & Weber, K. (2016). Chapter 5 - In Situ Observations of Airborne Ash From Manned Aircraft. In S. Mackie, K. Cashman, H. Ricketts, A. Rust, & M. Watson (Eds.), *Volcanic ash* (pp. 89–98). Elsevier. doi:https://doi.org/10.1016/B978-0-08-100405-0.00009-4

Emeis, S., Schäfer, K., & Münkel, C. (2008). Surface-based remote sensing of the mixing-layer height - A review. In *Meteorologische zeitschrift* (Vol. 17). doi:10.1127/0941-2948/2008/0312

Engelmann, R., Kanitz, T., Baars, H., Heese, B., Althausen, D., Skupin, A., ... Ansmann, A. (2016). The automated multiwavelength Raman polarization and water-vapor lidar PollyXT: The neXT generation. *Atmospheric Measurement Techniques*, *9*(4), 1767–1784. doi:10.5194/amt-9-1767-2016

Engler, C., Lihavainen, H., Komppula, M., Kerminen, V. M., Kulmala, M., & Viisanen, Y. (2007). Continuous measurements of aerosol properties at the Baltic Sea. *Tellus, Series B: Chemical and Physical Meteorology*, *59*(4), 728–741. doi:10.1111/j.1600-0889.2007.00285.x

Ester, M., Kriegel, H.-P., Sander, J., & Xu, X. (1996). A Density-Based Algorithm for Discovering Clusters in Large Spatial Databases with Noise.

Proceedings of the 2nd International Conference on Knowledge Discovery and Data Mining, 226–231. Retrieved from https://www.aaai.org/Papers/KDD/1996/KDD96-037.pdf

Franchi, G. G., Pacini, E., & Rottoli, P. (1984). Pollen grain viability in parietaria judaica l. During the long blooming period and correlation with meteorological conditions and allergic diseases". *Giornale Botanico Italiano*, *118*(3-4). doi:10.1080/11263508409426670

Freudenthaler, V., Esselborn, M., Wiegner, M., Heese, B., Tesche, M., Ansmann, A., ... Seefeldner, M. (2009). Depolarization ratio profiling at several wavelengths in pure Saharan dust during SAMUM 2006. *Tellus, Series B: Chemical and Physical Meteorology*, *61*(1), 165–179. doi:10.1111/j.1600-0889.2008.00396.x

Griffiths, P. T., Borlace, J. S., Gallimore, P. J., Kalberer, M., Herzog, M., & Pope, F. D. (2012). Hygroscopic growth and cloud activation of pollen: A laboratory and modelling study. *Atmospheric Science Letters*, *13*(4). doi:10.1002/asl.397

Groß, S., Freudenthaler, V., Wiegner, M., Gasteiger, J., Geiß, A., & Schnell, F. (2012). Dual-wavelength linear depolarization ratio of volcanic aerosols: Lidar measurements of the Eyjafjallajökull plume over Maisach, Germany. *Atmospheric Environment*, *48*, 85–96. doi:10.1016/j.atmosenv.2011.06.017

Groß, S., Tesche, M., Freudenthaler, V., Toledano, C., Wiegner, M., Ansmann, A., ... Seefeldner, M. (2011). Characterization of Saharan dust, marine aerosols and mixtures of biomass-burning aerosols and dust by means of multi-wavelength depolarization and Raman lidar measurements during SAMUM 2. *Tellus, Series B: Chemical and Physical Meteorology*, *63*(4). doi:10.1111/j.1600-0889.2011.00556.x

Gudmundsson, M. T., Thordarson, T., Hoskuldsson, A., Larsen, G., Bjornsson, H., Prata, F. J., ... Jonsdottir, I. (2012). Ash generation and distribution from the April-May 2010 eruption of Eyjafjallajökull, Iceland. *Scientific Reports*, *2*. doi:10.1038/srep00572

Guffanti, M., Casadevall, T. J., & Budding, K. E. (2010). *Encounters of aircraft with volcanic ash clouds: a compilation of known incidents, 1953-2009*. US Department of Interior, US Geological Survey. Retrieved from https://pubs.usgs.gov/ds/545/DS545.pdf

Haarig, M., Ansmann, A., Althausen, D., Klepel, A., Groß, S., Freudenthaler, V., ... Baars, H. (2017). Triple-wavelength depolarization-ratio profiling of Saharan dust over Barbados during SALTRACE in 2013 and 2014. *Atmospheric Chemistry and Physics*, *17*(17), 10767–10794. doi:10.5194/acp-17-10767-2017

Hair, J. W., Hostetler, C. A., Cook, A. L., Harper, D. B., Ferrare, R. A., Mack, T. L., ... Hovis, F. E. (2008). Airborne High Spectral Resolution Lidar for profiling Aerosol optical properties. *Applied Optics*, *47*(36). doi:10.1364/AO.47.006734

HALO PHOTONICS — StreamLine series - Product. (2021). Retrieved 2021-02-09, from https://halo-photonics.com/lidar-systems/

stream-line-series/

Harvey, N. J., Hogan, R. J., & Dacre, H. F. (2013). A method to diagnose boundary-layer type using doppler lidar. *Quarterly Journal of the Royal Meteorological Society*, *139*(676). doi:10.1002/qj.2068

Hey, J. V., Coupland, J., Foo, M. H., Richards, J., & Sandford, A. (2011). Determination of overlap in lidar systems. *Applied Optics*, *50*(30), 5791–5797. doi:10.1364/AO.50.005791

Hirsikko, A., O'Connor, E. J., Komppula, M., Korhonen, K., Pfüller, A., Giannakaki, E., ... Viisanen, Y. (2014). Observing wind, aerosol particles, cloud and precipitation: Finland's new ground-based remote-sensing network. *Atmospheric Measurement Techniques*, *7*(5), 1351–1375. doi:10.5194/amt-7-1351-2014

Hirtl, M., Arnold, D., Baro, R., Brenot, H., Coltelli, M., Eschbacher, K., ... Meinhard, D. (2020). A volcanic-hazard demonstration exercise to assess and mitigate the impacts of volcanic ash clouds on civil and military aviation. *Natural Hazards and Earth System Sciences*, *20*(6), 1719–1739. doi:10.5194/nhess-20-1719-2020

Hu, Y., Liu, Z., Winker, D., Vaughan, M., Noel, V., Bissonnette, L., ... McGill, M. (2006). Simple relation between lidar multiple scattering and depolarization for water clouds. *Optics Letters*, *31*(12), 1809. doi:10.1364/ol.31.001809

Hussein, T., Kukkonen, J., Korhonen, H., Pohjola, M., Pirjola, L., Wraith, D., ... Kulmala, M. (2007). Evaluation and modeling of the size fractionated aerosol particle number concentration measurements nearby a major road in Helsinki – Part II: Aerosol measurements within the SAPPHIRE project. *Atmospheric Chemistry and Physics*, *7*(15), 4081–4094. Retrieved from http://www.atmos-chem-phys.net/7/4081/2007/ doi:10.5194/acp-7-4081-2007

Illingworth, A. J., Barker, H. W., Beljaars, A., Ceccaldi, M., Chepfer, H., Clerbaux, N., ... Van Zadelhoff, G. J. (2015). The earthcare satellite : The next step forward in global measurements of clouds, aerosols, precipitation, and radiation. *Bulletin of the American Meteorological Society*, *96*(8). doi:10.1175/BAMS-D-12-00227.1

International Air Transport Association. (2010). IATA Economic Briefing - the Impact of Eyjafjallajokull'S Volcanic Ash Plume. *Middle East*(May). Retrieved from https://www.iata.org/en/iata-repository/publications/economic-reports/impact-of-ash-plume/

IPCC. (2013). *Climate Change 2013: The Physical Science Basis. Contribution of Working Group I to the Fifth Assessment Report of the Intergovernmental Panel on Climate Change*. Cambridge, United Kingdom and New York, NY, USA: Cambridge University Press. doi:10.1017/CBO9781107415324

Jiang, X.-Q., Mei, X.-D., & Feng, D. (2016, jan). Air pollution and chronic airway diseases: what should people know and do? *Journal of thoracic disease*, *8*(1), E31–40. doi:10.3978/j.issn.2072-1439.2015.11.50

Kanitz, T., Ansmann, A., Engelmann, R., & Althausen, D. (2013). North-south cross sections of the vertical aerosol distribution over the At-

lantic Ocean from multiwavelength Raman/polarization lidar during Polarstern cruises. *Journal of Geophysical Research Atmospheres*, *118*(6). doi:10.1002/jgrd.50273

Kanitz, T., Seifert, P., Ansmann, A., Engelmann, R., Althausen, D., Casiccia, C., & Rohwer, E. G. (2011). Contrasting the impact of aerosols at northern and southern midlatitudes on heterogeneous ice formation. *Geophysical Research Letters*, *38*(17). doi:10.1029/2011GL048532

Kaspari, S., Skiles, S. M. K., Delaney, I., Dixon, D., & Painter, T. H. (2015). Accelerated glacier melt on Snow Dome, Mount Olympus, Washington, USA, due to deposition of black carbon and mineral dust from wildfire. *Journal of Geophysical Research*, *120*(7), 2793–2807. doi:10.1002/2014JD022676

Katifori, E., Alben, S., Cerda, E., Nelson, D. R., & Dumais, J. (2010). Foldable structures and the natural design of pollen grains. *Proceedings of the National Academy of Sciences of the United States of America*, *107*(17). doi:10.1073/pnas.0911223107

Koch, D., Menon, S., Del Genio, A., Ruedy, R., Alienov, I., & Schmidt, G. A. (2009). Distinguishing aerosol impacts on climate over the past century. *Journal of Climate*, *22*(10), 2659–2677. doi:10.1175/2008JCLI2573.1

Kulmala, M., Hämeri, K., Aalto, P. P., Mäkelä, J. M., Pirjola, L., Douglas Nilsson, E., ... O'Dowd, C. D. (2001). Overview of the international project on biogenic aerosol formation in the boreal forest (BIOFOR). *Tellus, Series B: Chemical and Physical Meteorology*, *53*(4), 324–343. doi:10.3402/tellusb.v53i4.16601

Leskinen, M., Markkula, I., Koistinen, J., Pylkkö, P., Ooperi, S., Siljamo, P., ... Tiilikkala, K. (2011). Pest insect immigration warning by an atmospheric dispersion model, weather radars and traps. *Journal of Applied Entomology*, *135*(1-2), 55–67. doi:10.1111/j.1439-0418.2009.01480.x

Liou, K.-N., & Schotland, R. M. (1971). Multiple Backscattering and Depolarization from Water Clouds for a Pulsed Lidar System. *Journal of the Atmospheric Sciences*, *28*(5). doi:10.1175/1520-0469(1971)028<0772:mbadfw>2.0.co;2

Mamouri, R. E., & Ansmann, A. (2017). Potential of polarization/Raman lidar to separate fine dust, coarse dust, maritime, and anthropogenic aerosol profiles. *Atmospheric Measurement Techniques*, *10*(9). doi:10.5194/amt-10-3403-2017

Manninen, A. J., O'Connor, E. J., Vakkari, V., & Petäjä, T. (2016). A generalised background correction algorithm for a Halo Doppler lidar and its application to data from Finland. *Atmospheric Measurement Techniques*, *9*(2), 817–827. doi:10.5194/amt-9-817-2016

Maso, M. D., Hyvärinen, A., Komppula, M., Tunved, P., Kerminen, V.-M., Lihavainen, H., ... Kulmala, M. (2008). Annual and interannual variation in boreal forest aerosol particle number and volume concentration and their connection to particle formation. *Tellus B: Chemical and Physical Meteorology*, *60*(4), 495–508. doi:10.1111/j.1600-0889.2008.00366.x

McCormick, M. P., Thomason, L. W., & Trepte, C. R. (1995). Atmospheric effects of the Mt Pinatubo eruption. *Nature*, *373*(6513).

doi:10.1038/373399a0

Middleton, N. J. (2017). Desert dust hazards: A global review. *Aeolian Research*, *24*, 53–63. doi:https://doi.org/10.1016/j.aeolia.2016.12.001

Müller, D., Ansmann, A., Mattis, I., Tesche, M., Wandinger, U., Althausen, D., & Pisani, G. (2007). Aerosol-type-dependent lidar ratios observed with Raman lidar. *Journal of Geophysical Research Atmospheres*, *112*(16). doi:10.1029/2006JD008292

Myhre, G., Myhre, C. E. L., Samset, B. H., & Storelvmo, T. (2015). Aerosols and their Relation to Global Climate and Climate Sensitivity. *Nature Education*, *4*(5). Retrieved from https://www.nature.com/scitable/knowledge/library/aerosols-and-their-relation-to-global-climate-102215345/

O'Connor, E. J., Illingworth, A. J., Brooks, I. M., Westbrook, C. D., Hogan, R. J., Davies, F., & Brooks, B. J. (2010). A method for estimating the turbulent kinetic energy dissipation rate from a vertically pointing Doppler lidar, and independent evaluation from balloon-borne in situ measurements. *Journal of atmospheric and oceanic technology*, *27*(10), 1652–1664. doi:10.1175/2010JTECHA1455.1

Papagiannopoulos, N., Mona, L., Amodeo, A., D'Amico, G., Gumà Claramunt, P., Pappalardo, G., ... Wiegner, M. (2018). An automatic observation-based aerosol typing method for EARLINET. *Atmospheric Chemistry and Physics*, *18*(21). doi:10.5194/acp-18-15879-2018

Pearson, G., Davies, F., & Collier, C. (2009). An analysis of the performance of the UFAM pulsed Doppler lidar for observing the boundary layer. *Journal of Atmospheric and Oceanic Technology*, *26*(2), 240–250. doi:10.1175/2008JTECHA1128.1

Prata, A. J., Carn, S. A., Stohl, A., & Kerkmann, J. (2007). Long range transport and fate of a stratospheric volcanic cloud from Soufrière Hills volcano, Montserrat. *Atmospheric Chemistry and Physics*, *7*(19). doi:10.5194/acp-7-5093-2007

Putaud, J. P., Van Dingenen, R., Alastuey, A., Bauer, H., Birmili, W., Cyrys, J., ... Raes, F. (2010). A European aerosol phenomenology - 3: Physical and chemical characteristics of particulate matter from 60 rural, urban, and kerbside sites across Europe. *Atmospheric Environment*, *44*(10). doi:10.1016/j.atmosenv.2009.12.011

Raman, C. V., & Krishnan, K. S. (1928). A New Type of Secondary Radiation. *Nature*, *121*(3048), 501–502. doi:10.1038/121501c0

Reynolds, R. L., Goldstein, H. L., Moskowitz, B. M., Kokaly, R. F., Munson, S. M., Solheid, P., ... Derry, J. (2020, apr). Dust Deposited on Snow Cover in the San Juan Mountains, Colorado, 2011–2016: Compositional Variability Bearing on Snow-Melt Effects. *Journal of Geophysical Research: Atmospheres*, *125*(7). doi:10.1029/2019JD032210

Sassen, K., & Petrilla, R. L. (1986). Lidar depolarization from multiple scattering in marine stratus clouds. *Applied Optics*, *25*(9), 1450. doi:10.1364/ao.25.001450

Seinfeld, J. H., & Pandis, S. N. (2016). *Atmospheric chemistry and physics:*

from air pollution to climate change. John Wiley & Sons, New York.

Stohl, A., Prata, A. J., Eckhardt, S., Clarisse, L., Durant, A., Henne, S., ... Weinzierl, B. (2011). Determination of time-and height-resolved volcanic ash emissions and their use for quantitative ash dispersion modeling: The 2010 Eyjafjallajökull eruption. *Atmospheric Chemistry and Physics*, *11*(9). doi:10.5194/acp-11-4333-2011

Tesche, M., Gross, S., Ansmann, A., Müller, D., Althausen, D., Freudenthaler, V., & Esselborn, M. (2011). Profiling of Saharan dust and biomass-burning smoke with multiwavelength polarization Raman lidar at Cape Verde. *Tellus, Series B: Chemical and Physical Meteorology*, *63*(4). doi:10.1111/j.1600-0889.2011.00548.x

Vakkari, V., Baars, H., Bohlmann, S., Bühl, J., Komppula, M., Mamouri, R.-E., & O'Connor, E. J. (2020). Aerosol particle depolarization ratio at 1565nm measured with a Halo Doppler lidar. *Atmospheric Chemistry and Physics Discussions*, *2020*, 1–28 [preprint]. doi:10.5194/acp-2020-906

Vakkari, V., Manninen, A. J., O'Connor, E. J., Schween, J. H., Van Zyl, P. G., & Marinou, E. (2019). A novel post-processing algorithm for Halo Doppler lidars. *Atmospheric Measurement Techniques*, *12*(2), 839–852. doi:10.5194/amt-12-839-2019

Weitkamp, C. (2005). *Lidar : range-resolved optical remote sensing of the atmosphere* (Vol. 102). Springer-Verlag, New York.

Winker, D. M., Vaughan, M. A., Omar, A., Hu, Y., Powell, K. A., Liu, Z., ... Young, S. A. (2009). Overview of the CALIPSO mission and CALIOP data processing algorithms. *Journal of Atmospheric and Oceanic Technology*, *26*(11). doi:10.1175/2009JTECHA1281.1

Yang, S., Xu, B., Cao, J., Zender, C. S., & Wang, M. (2015). Climate effect of black carbon aerosol in a Tibetan Plateau glacier. *Atmospheric Environment*, *111*, 71–78. doi:10.1016/j.atmosenv.2015.03.016